Science
AAAS

Supplementary Materials for

Human POT1 protects the telomeric ds-ss DNA junction by capping the 5′ end of the chromosome

Valerie M. Tesmer *et al*.

Corresponding author: Jayakrishnan Nandakumar, jknanda@umich.edu

Science **381**, 771 (2023)
DOI: 10.1126/science.adi2436

The PDF file includes:

Other Supplementary Material for this manuscript includes the following:

Materials and Methods

Primers, plasmids, cloning, and mutagenesis

All DNA oligonucleotides used in cloning, EMSAs, FISH, and crystallography were purchased from Integrated DNA Technologies (IDT). See table S2 for details of oligonucleotides used in this study. The pCW22_TREtight_MCS_UBC_rtTA_IRES_Blast lentiviral vector for dox-inducible expression in HEK 293E cells was a kind gift from Dr. Joachim Lingner (*34*). Plasmids used in this study and described elsewhere: pFBHTb-Smt3star-hPOT1 and pFBHTb-Smt3star-hTPP1N for High Five insect cell expression of hPOT1 and hTPP1N, respectively (*44*). hDBD protein for biochemical and crystallographic experiments was expressed from a pFBHTb-Smt3star-hPOT1-1-299 plasmid obtained by restriction-based cloning of the hPOT1 open reading frame (ORF) into the BamHI/XhoI sites of the pFBHTb-Smt3star vector. His_6-Smt3-tagged mouse POT1a DBD and POT1b DBD constructs for *E. coli* expression were obtained by restriction-based cloning into the BamHI/XhoI sites of the pSmt3 vector (MTA with Cornell University; (*45*)). The dox-inducible hPOT1 lentiviral expression plasmid was constructed by amplifying hPOT1-6X-Myc from the pcDNA3-hPOT1-6X-Myc plasmid (*46*) and cloning it between the HpaI/PacI sites of the pCW22_TREtight_MCS_UBC_rtTA_IRES_Blast vector. The resulting plasmid was named pTet-CW22-hPOT1-6X-Myc. Mutations in plasmids encoding WT ORFs were introduced with the QuikChange® Site-Directed Mutagenesis Kit (Agilent Technologies) using complementary mutagenic primers. Sequential rounds of mutagenesis were performed for generating constructs containing multiple mutations within the same cDNA construct. Transformations of lentiviral plasmids to obtain plasmid DNA were performed in the recombination-compromised *E. coli* Stable strain (New England Biolabs). Transformations for all other plasmid preparations were performed in *E. coli* XL10-Gold cells (Agilent). All new plasmids described here were sequenced to confirm the presence of the intended mutation and the absence of errors introduced during the process of cloning.

Recombinant protein expression and purification

Full-length hPOT1 was co-expressed with human TPP1N (aa 87-334) by baculoviral coinfection of insect cells and their complex was purified as described previously (*44*). The DNA binding domain of human POT1 WT and variants were expressed as His_6-SUMOstar-DBD fusion proteins in High Five cells (BTI-Tn-5B1-4) via the Bac-to-Bac baculovirus system (Thermo Fisher Scientific). Approximately 40 h after viral infection at 28ºC, cells from 0.5-4.5 L of culture were harvested and processed immediately or stored at -80ºC until further use. Based on pellet size, cells were resuspended in 40-120 ml lysis buffer containing 25 mM Tris (pH 8), 500 mM NaCl, 10 mM 2-mercaptoethanol, 0.1 mM EDTA, 1 mM PMSF, and one tablet of cOmplete mini, EDTA-free protease inhibitor cocktail (Roche; 11836170001) and lysed by sonication. The lysate was clarified by centrifugation followed by filtration through glass fiber filters. His-tagged protein was purified by batch method with a 2 h nutation at 4ºC using ~1 ml of Ni-NTA agarose resin (Qiagen) per L of culture. After extensive washes with buffer A (25 mM Tris (pH 8), 500 mM NaCl, and 10 mM 2-mercaptoethanol), including a wash containing 10 mM imidazole, the protein was eluted with 150 mM imidazole in buffer A. The N-terminal His_6-SUMOstar tag was removed using SUMOstar protease added to 1-2% and digestion performed along with dialysis for 1 h in buffer containing 25 mM Tris (pH 8), 150 mM NaCl, and 10 mM 2-mercaptoethanol. The NaCl concentration was then increased to 300-500 mM and size-exclusion chromatography was performed on an AKTA PURE FPLC system (Cytiva) using a HiLoad 16/600 Superdex S75 pg column equilibrated with 25 mM Tris (pH 8), 500 mM NaCl,

and 2 mM dithiothreitol (DTT). DBD-containing fractions were pooled and concentrated on an Amicon Ultra-4 Ultracel (10,000 Da or 30,000 Da cutoff) to 2-10 mg/ml. WT hDBD yielded up to 10-15 mg pure protein per L of culture. DNA binding domains of mouse POT1a (and its variants) and POT1b were expressed as His_{10}-Smt3-DBD fusion proteins in *E. coli* BL21(DE3) cells. Log phase LB cultures were induced with 100 µM IPTG and harvested after overnight expression at 16ºC. Mouse POT1a and POT1b DBD WT and variants were purified using a scheme like that used for insect-expressed hDBD with the following exceptions: the bacterial cells required greater sonication time (5-6 min versus 2 min) and amplitude (70% vs 50%) for lysis; mouse His_{10}-Smt3 tagged proteins were eluted from Ni-NTA agarose with 300 mM imidazole in buffer A, and the His_{10}-Smt3 tag was cleaved off with Ulp1 protease. Both POT1a and POT1b DBD proteins yielded approximately 0.5 mg protein per L of culture, with degradation products apparent for POT1b DBD. Protein quantitation and quality were established by Bradford analysis (Bio-Rad; cat #S5000006) and Coomassie blue staining of SDS-PAGE gels, respectively. For the latter, purified proteins were run on 4-15% Mini-PROTEAN TGX precast gels (Bio-Rad; 4561085) alongside the Precision Plus Protein Dual Color Standard (Bio-Rad; 161-0374).

Electrophoretic Mobility Shift Assays

Oligonucleotides were 5'-end-labeled with γ-^{32}P-ATP (Perkin Elmer; BLU502A250UC) and T4 polynucleotide kinase (New England Biolabs; M0201S). Reactions were quenched with EDTA followed by heating the samples to 65ºC for 5 min. The unincorporated label was removed on Micro Bio-Spin P-6 gel columns (Bio-Rad; 7326221) pre-equilibrated in 10 mM Tris (pH 8) and 1 mM EDTA. Proteins and labeled DNA were diluted and incubated in a binding reaction with a filtered buffer consisting of 20 mM Tris (pH 8), 100 mM NaCl, 10 µg/ml bovine serum albumin, 1 µg/ ml *E. coli* tRNA (Roche; 10109541001), and 7% glycerol. The concentration of radiolabeled DNA used in the experiment was kept at least threefold to tenfold under the lowest protein concentration, with the exact concentrations noted in the figure legends. For competition analysis, unlabeled oligonucleotides were included with the radiolabeled oligonucleotide before the addition of protein. Binding reactions were incubated on ice for approximately 15 min before resolution on a 6% polyacrylamide-0.5X TBE gel run on ice with prechilled 0.5X TBE buffer. The dried gel was exposed to a Phosphorimager screen for imaging on the Typhoon Phosphorimager (Cytiva) and quantitation of the free and bound DNA was performed with ImageQuant (Cytiva) using rolling ball background correction. Data and graphical analysis from at least three independently run experiments were performed using Microsoft Excel and Prism Graphpad. The reported K_d was constrained to be a shared value for at least three independent experiments analyzed by nonlinear fit and specific binding.

Formation of hDBD-DNA complexes for crystallization

For the hDBD complex with 5'-P-hp-ss$^{1\text{-}12}$, the concentration of NaCl was lowered to 260 mM, and 3.3 mg of protein was incubated with 760 µg DNA (1.2-fold molar excess of DNA) on ice for 10 min. For the hDBD complex with 5'-P-ds-ss$^{1\text{-}12}$, the oligonucleotides Anchor(10ds)ss$^{1\text{-}12}$ and 5'-P-Anchor(10ds)-C_strand were first annealed using a 1.2-fold excess of the C strand (1.4 mg and 0.8 mg, respectively). The oligonucleotides were heated to approximately 95ºC and slow-cooled to room temperature in 25 mM Tris (pH 8) and 50 mM NaCl. 5 mg of hDBD was added (a binding reaction with a 1.3-fold molar excess of DNA), reducing the NaCl concentration to 220 mM and incubating on ice for 10 min. Each nucleoprotein complex was

purified on the AKTA PURE FPLC system using a Superdex 200 10/300 GL column equilibrated in 25 mM Tris (pH 8), 100 mM NaCl, and 2 mM DTT. Peak fractions were concentrated on an Amicon Ultra-4 Ultracel (30,000 Da cutoff) to 13-14 mg/ml, yielding 2 mg of the complex that was subjected directly to crystallization trials.

hDBD-DNA crystallization and crystal harvesting

hDBD complex with 5'-P-hp-ss$^{1-12}$ was crystallized at 16ºC by the hanging drop method in a drop containing 0.8 µl of 13 mg/ml protein-DNA complex (in 25 mM Tris (pH 8), 100 mM NaCl, and 2 mM DTT) and 0.8 µl well solution (0.1 M NaOAc (pH 5.2) and 10% PEG 20,000). Crystals were harvested in 25 mM Tris (pH 8), 100 mM NaCl, 0.1 M NaOAc (pH 5.2), and 10% PEG 20,000 and cryoprotected in harvesting solution supplemented with 30% ethylene glycol.

hDBD complex with 5'-P-ds-ss$^{1-12}$ was crystallized at 16ºC by the sitting drop method in a drop containing 0.5 µl 14 mg/ml protein-DNA complex (in 25 mM Tris (pH 8), 100 mM NaCl, and 2 mM DTT) and 0.5 µl well solution (0.02 M $MgCl_2$, 0.9 M Hepes (pH 7.5), and 20% polyacrylic acid N100 sodium salt, derived from condition G2 of the JCSG+ screen (NeXtal; 130720). Crystals were harvested in 25 mM Tris (pH 8), 100 mM NaCl, 0.02 M $MgCl_2$, 0.1 M Hepes (pH 7.5), and 22% polyacrylic acid N100 sodium salt and cryoprotected in harvesting solution supplemented with 35% ethylene glycol.

hDBD-DNA structure determination

Diffraction data for crystals of the hDBD-5'-P-hp-ss$^{1-12}$ complex and the hDBD-5'-P-ds-ss$^{1-12}$ complex were obtained at Argonne National Laboratory on LS-CAT beamline 21 ID-D at a wavelength of 1.127 Å and a temperature of 100 K. Mosflm (*47*) was used to index and integrate data and Aimless was used for data reduction using the CCP4i interface (*48*). Molecular replacement was performed in Phaser (*49*) within the PHENIX suite (*50*) using hDBD from the previously solved structure with ss DNA (PDB accession code: 1XJV) as a search model (*7*). Preliminary rigid body and restrained refinement were performed in PHENIX to generate $2F_o$ - F_c maps that showed clear density for DNA, which was built manually in Coot (*51*). The hDBD-5'-P-ds-ss$^{1-12}$ diffraction was highly anisotropic as the data showed a CC(1/2) > 0.20 to 2.6 Å along the reciprocal k-axis, but only to 3.17 Å and 3.17 Å along the h- and l-axes, respectively. Therefore, this structure was refined to 3.0 Å initially. Iterative model building in Coot and restrained refinement in PHENIX Refine were performed for both structures. Towards the final stages of model building, ordered water molecules were placed in the model during refinement in PHENIX and model building in Coot. The final round of refinement and model building for hDBD-5'-P-ds-ss$^{1-12}$ was performed at 2.6 Å using strict geometric restraints to include data at higher resolution without over-refinement (the spread between R_{work}/R_{free} was used to monitor model bias/over-refinement). The final structural model for the hDBD-5'-P-hp-ss$^{1-12}$ complex contained hPOT1 aa 6-299 and all nucleotides of the DNA. The final structural model for the hDBD-5'-P-ds-ss$^{1-12}$ complex contained hPOT1 aa 6-298 and all nucleotides of the DNA. Three ordered acetate ions from the crystallization conditions were built into density for the hDBD-5'-P-hp-ss$^{1-12}$ structure. The final structural models displayed excellent geometry as evidenced by Molprobity Analysis (hDBD-5'-p-hp-ss$^{1-12}$: Molprobity score = 1.26 (100th percentile); hDBD-5'-P-ds-ss$^{1-12}$: Molprobity score = 1.6 (99th percentile)). See table S1 for detailed data statistics and the PDB validation reports in the other supplementary materials. Both structures aligned closely with each other (RMSD = 1.0 Å). One notable difference in the protein chain was POT1 loop aa 251-258, which occupied different conformations in the two structures, dictated by

crystal packing. The DNA nucleotide G^2 was flipped in towards hDBD, forming H-bonds with hDBD S99 in the hDBD-5'-P-ds-ss^{1-12}. In contrast, an acetate ion in the hDBD-5'-p-hp-ss^{1-12} structure H-bonds S99 while G^2, which occupies a flipped-out conformation, does not interact with hPOT1. Structure images were generated in PyMOL (*52*).

In vitro 5′ DNA end protection assay

A 3'-IRDye 800 CW-labeled DNA substrate that mimics the telomeric junction containing a 3'-overhang was created as follows: 1.0 µM Anchor(10ds)ss^{1-12} was annealed with a slight excess (1.3 µM) of 5'-P-Anchor(10ds)-C_strand/IRDye 800CW (IRDye 800CW fluorophore-labeled at the 3'-end) in a 100 µl reaction containing 10 mM Tris (pH 8) and 50 mM NaCl. The annealing reaction was heated to approximately 95°C and slow-cooled to room temperature, and stored in aliquots at -20°C. For the reaction, a fresh 20 nM DNA stock was prepared in 1X λ-exonuclease buffer (67 mM glycine-KOH, 2.5 mM $MgCl_2$, 50 µg/ml BSA at pH 9.4, supplied with λ-exonuclease enzyme; NEB; M0262S). A fresh 500 nM DBD protein stock (determined by Bradford analysis) was prepared in 25 mM Tris (pH 8) and 500 mM NaCl. 5 µl of 20 nM DNA was placed in each reaction tube with 1 µl of 500 nM DBD or protein dilution buffer alone and incubated on ice for 10 min (unless mentioned otherwise) in the dark. A dilution of 0.1 U/µl of λ-exonuclease was prepared in 1X λ-exonuclease buffer supplemented with 16% glycerol. Appropriate samples were supplemented with 4 µl of the λ-exonuclease (0.4 U) or its buffer control and the 10 µl reactions were incubated for 10 min at room temperature. The reactions were then moved to ice and quenched with 2.5 mM EDTA before native gel analysis on a 6% polyacrylamide-0.5X TBE gel run on ice, as described above for EMSA analysis. Samples that were examined by denaturing gels were supplemented with an equal volume of formamide loading dye before heating at 95°C for 5 min and rapid cooling on ice. Denatured samples were run alongside a hydrolyzed RNA ladder on a gel containing 20% polyacrylamide, 8M urea, and 1X TBE for 90 min at 250 V. Imaging and quantitation were performed using the LI-COR Odyssey FC imager and associated software.

Human cell culture

The inducible *POT1* KO HEK 293E cell line was a kind gift from Dr. Joachim Lingner (*34*). This cell line and all derivatives, and HEK 293T cells (used to generate lentiviruses; ATCC; CRL-3216) were cultured at 37°C in the presence of 5% CO_2 and propagated in modified DMEM (Dulbecco's Modified Eagle Medium; Gibco 11995-065) containing 100 U/ml penicillin, 100 µg/ml streptomycin, and 10% Tet system approved fetal bovine serum (Gibco A4736401).

Generation of lentiviruses

pTet-CW22-hPOT1-6X-Myc (WT or mutant, 1.76 µg) and packaging vectors pMDLg/pRRE (1.16 µg), pRSV-Rev (0.44 µg), and pMD2.G (0.64 µg) were used to generate hPOT1-6X-Myc WT- and mutant-encoding lentiviruses to transduce the inducible *POT1* KO HEK 293E cell line. For preparing lentiviruses, the above plasmid mixture was transfected into HEK 293T cells (ATCC) at 60% confluency in a 6-well format using Lipofectamine LTX (Thermo Scientific; 15338100). The supernatant containing virus particles was collected after 24 and 48 h, pooled, and concentrated using the LentiX concentrator (Takara Bio; PT4421-2). The concentrated viral particles were added to 50% confluent HEK 293E cells in a 6-well format, along with Polybrene (8 µg/ml; EMD Millipore; TR1003). The medium was replaced with regular growth medium the

next day. After transduction of the human cell line, infected cells were selected with 8 μg/ml blasticidin, along with a kill control. Clonal cell lines for selected HEK 293E stable cell populations were isolated by single-cell dilution into a 96-well plate. Isolated clones were validated by immunoblotting for Myc-POT1 and TIF analysis following consecutive treatment with 4-OHT (3 days) and dox (4 days).

Immunoblotting

Immunoblotting was performed as described in previous studies (*46, 53*). The following antibodies were used for detection with chemiluminescence by ECL plus reagents (Pierce ECL Western Blotting Substrate; Thermo Scientific; 34580), mouse monoclonal anti-c-Myc (9E10) HRP conjugate (Santa Cruz; sc-40 HRP; 1:10,000; RRID of unconjugated antibody: AB_2266850), mouse monoclonal anti-β-actin antibody (Sigma; A5441; 1:10,000; RRID: AB_476744), and anti-mouse HRP conjugated secondary antibody (Jackson Immunoresearch; 715-035-150; RRID: AB_2340770). The data were visualized using a gel-documentation system (LI-COR Odyssey FC imager).

TRF analysis

POT1 KO HEK 293E clonal cell lines were treated with 0.5 μM 4-OHT (Sigma) for 3 d to KO endogenous *POT1*. Dox was then added at 1 μg/ml for 4 d to induce POT1-Myc expression. Genomic DNA was isolated from 0.5-2 million cells using the GenElute Mammalian Genomic DNA Miniprep Kit (Sigma; G1N350). 3-4 μg of DNA was digested with frequent cutters HinfI and RsaI and incubated overnight at 37°C. The DNA digest was run on a 10 cm long 0.7% agarose-1X TAE gel along with a λ DNA-HindIII digest ladder (NEB; N3012S) at a constant 70 V for ~3 h. The gel was transferred to a sheet of dry Whatman filter paper and dried at 50°C for 1.5 h. The dried gel was prehybridized in hybridization solution (5X SSC buffer, 5X Denhardt's Solution (Bioworld; 10750005-2), 10 mM Na_2HPO_4, and 1 mM $Na_2H_2P_2O_7$) at 42°C with rotation in a hybridization oven for at least 10 min and then hybridized with a 5'-^{32}P-labeled telomeric C-probe $(CTAACC)_4$ overnight (*54*). Post hybridization, the gel was washed once with 2X SSC for 15 min, thrice with 0.1X SSC/0.1% SDS for 10 min each, and exposed to a Phosphorimager screen for 24-120 h. The native gel representing the G-rich overhang was visualized on an Amersham Typhoon Biomolecular imager. To measure total telomere length, the gel was denatured in buffer containing 0.5 M NaOH for 20 min, washed with water for 10 min, neutralized in buffer containing 0.5 M Tris HCl (pH 8) for 15 min, and washed again in water for 10 min. The denatured gel was prehybridized, hybridized, washed, and visualized as described above to determine the total telomere signal (exposure time of 1-24 h).

STELA-based determination of the 5'-terminal nucleotide in human cell lines

The 5'-terminal nucleotide was determined by adapting the STELA-based method described previously (*22, 23*). Briefly, 1 μg of fresh genomic DNA was digested with 20 U EcoRI-HF (NEB; R3101S) in a 20 μl reaction for 2-4 h at 37ºC. In six separate tubes, 10 ng of digested DNA was incubated with 1 nM of each telorette and 0.5 μl (or 200 units) T4 DNA ligase (NEB; M0202S) in a 10 μl reaction with the provided ligation buffer for 12 h at 35 ºC. 1 ng of each ligated sample was PCR-amplified in a 25 μl reaction containing 0.5 μl 10 μM XpYpE2 primer, 0.5 μl 10 μM Teltail primer, 12.5 μl Failsafe PCR buffer H, and 0.8 μl Failsafe enzyme mix (2.5 U/μl; Biosearch Technologies; FSE51100). The PCR was initiated with a denaturation step at 94ºC for 15 s, followed by 25 cycles comprising incubations at 95ºC for 15 s, 58ºC for 20 s and

68ºC for 10 min, and terminated with a final extension of 68ºC for 10 min. 5 µl of 6X DNA loading dye (30% glycerol, 0.25% bromophenol blue, and 0.25 % xylene cyanol) was added to each sample and 12 µl was resolved on a 0.7% agarose-1X TAE mini-gel run for 1 h at 100 V. The gel was denatured, dried, and neutralized before in-gel probing overnight with ^{32}P-end-labeled XpYpB2 primer following the protocol detailed for TRF analysis (*54*).

TIF analysis

POT1 KO HEK 293E (population and clonal) cell lines were treated with 0.5 µM 4-OHT (Sigma) for 3 (clonal) or 4 (population) d to KO endogenous *POT1*. Dox was then added at 1 µg/ml for 3 (population) or 4 (clonal) d to induce POT1-Myc expression, with cells being plated on coverslips 6 days post-4-OHT addition. Fixed cells were permeabilized in 0.5% NP-40, 1X PBS for 10 min at RT and washed twice in 1X PBS. Cells were then rehydrated in 50% Formamide - 2X SSC (saline-sodium citrate) for 5 min. A hybridization solution of the following composition was prepared: 100 mg/ml dextran sulfate, 0.125 mg/ml *E. coli* tRNA, 1 mg/ml nuclease-free BSA, 0.5 mg/ml salmon sperm DNA, 1 mM vanadyl ribonucleoside complexes, and 50% formamide in 2X SSC. Coverslips with cells facing down were incubated in hybridization solution supplemented with 0.05 µM (0.3 µg/ml) Cy3-labelled PNA-$(CCCTAA)_3$ telomeric C probe (PNA Bio; F1002). The coverslips were hybridized at 80°C on a heat block for 6 min and incubated in the dark for 2 h. They were then washed twice with 50% formamide - 2X SSC for 30 min, twice with 1X PBS, fixed again with 4% paraformaldehyde, 1X PBS for 10 min, and washed thrice with 1X PBS before being processed for IF. Coverslips were blocked in blocking buffer (1 mg/ml BSA, 3% goat serum, 0.1% Triton-X 100, and 1 mM EDTA (pH 8)) for 30 min, incubated with anti-c-Myc antibody, mouse monoclonal (SP2) (Developmental Studies Hybridoma Bank; 9E10; 1:500; RRID: AB_2266850) to visualize C-terminally 6X-Myc-tagged hPOT1 along with anti-53BP1 rabbit primary antibody (Novus Biologicals; NB100-304; 1:1000; RRID:AB_10003037) for 1 h at RT, and washed thrice in 1X PBS. Coverslips were then incubated with goat anti-mouse secondary antibody conjugated to Alexa Fluor 488 (Life Technologies; A28175; 1:500; RRID: AB_2536161), and goat anti-rabbit secondary antibody conjugated to Alexa Fluor 647 (Life Technologies; A21244; 1:500; RRID:AB_2535812) for 30 min at RT, washed thrice in PBS, mounted on microscope slides with ProLong Gold antifade reagent with DAPI (Life Technologies; 8961S), and sealed with clear nail polish. The mounted coverslips were imaged using a laser scanning confocal microscope (SP5; Leica, Germany) equipped with a 100X oil objective. The immunofluorescence-fluorescence in situ hybridization (IF-FISH) image data were processed with ImageJ and Adobe Photoshop, and colocalizations were quantified manually. We used n = 50-75 nuclei for each sample as similar numbers were sufficient in previous studies to reveal phenotypic differences. Nuclei were selected for TIF analysis if they had at least 10-15 visible telomere FISH foci and punctate hPOT1-Myc foci colocalizing with them. Note that nuclei were selected without knowledge of the 53BP1 signal (i.e., blind towards 53BP1 status). This was done to eliminate bias from selecting cells because of their DNA damage marker expression status.

Replicates

In vitro experiments are considered technical replicates by default even when separate transformations/transfections were performed to generate purified proteins as no living biological specimen was being analyzed. For experiments from cultured human cells, those involving independently isolated clones are biological replicates; the replicates with cell populations use

the same parental cell lines and are, therefore, described as technical replicates even if they involve separate viral transduction or 4-OHT or dox treatments.

Supplementary Figures S1 to S13 and Supplementary Tables S1 and S2

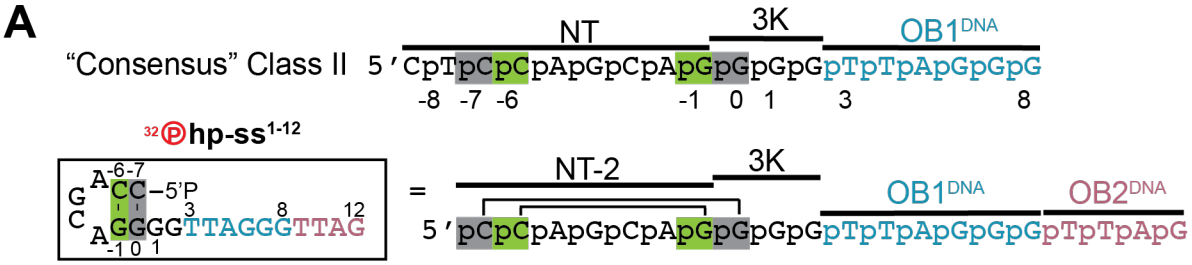

Fig. S1. Reanalysis of published POT1-SELEX data. (**A**) *Top:* Previously published SELEX binding *Class II* for hPOT1 with phosphodiester groups depicted as a "p" between contiguous nucleotides to highlight the presence of a 5'-phosphodiester attached to the telomeric 5'-C (shaded grey) within the identified SELEX hits (*24*). The terminal 5'-P that naturally exists at a telomeric junction is mimicked by the phosphodiester group connecting $^{-8}$T and $^{-7}$C in the SELEX *Class II* hits. *Bottom:* The predicted hp (boxed) and linear structures of 5'-P-hp-ss$^{1-12}$ used in EMSA and crystallography are shown. (**B**) Predicted folding of previously published SELEX *Class II* hits. The telomeric junction base-pair is shaded grey and non-telomeric base-pairs are in shades of green.

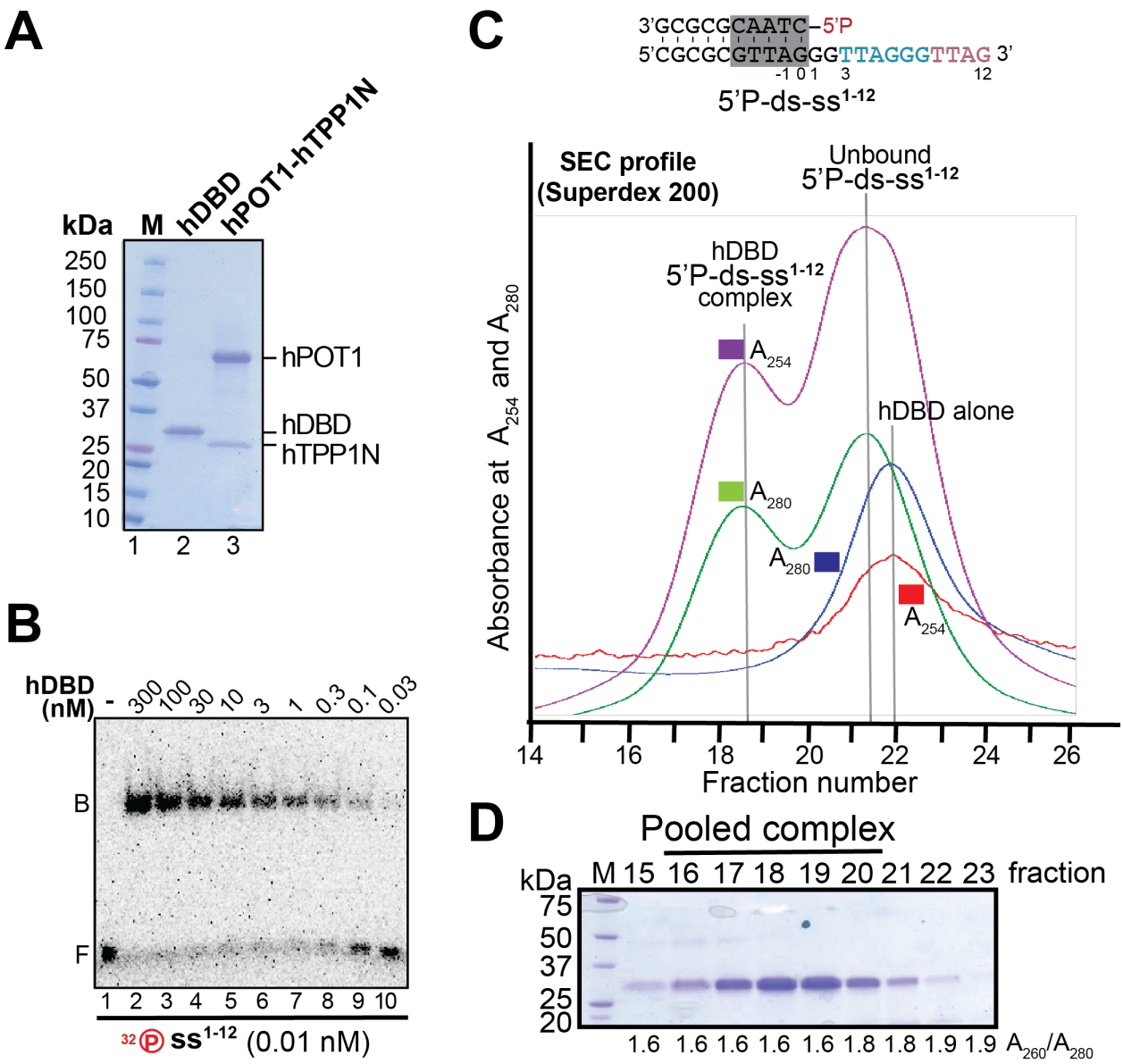

Fig. S2. Human POT1 binds a ds-ss junction in vitro. (**A**) Coomassie-stained SDS-PAGE showing hDBD and human POT1-TPP1N that were purified from baculovirus-infected insect cells and used in the DNA-binding analysis. (**B**) EMSA showing binding of hDBD with a ss DNA containing two telomeric GGTTAG repeats (5'-P-ss$^{1-12}$); DNA at 0.01 nM; n=3. (**C**) Due to DNA duplex instability at sub-nanomolar concentrations, we were unable to perform K_d determination using EMSA analysis with the two-stranded 5'-P-ds-ss$^{1-12}$ (10 bp total ds region) that was used in crystallography. Instead, we characterized this hDBD-DNA complex using size-exclusion chromatography (SEC) using micromolar-range concentrations of the DNA (and protein). The SEC profile using a Superdex 200 column (Cytiva) of hDBD alone and a mixture of hDBD and a stoichiometric excess of 5'-P-ds-ss$^{1-12}$ is shown. Absorbance at 280 nm (A_{280}) and 254 nm (A_{254}) was plotted to identify peaks containing protein-only, DNA-only, or a protein-DNA complex; n=1. (**D**) Coomassie blue-stained SDS-PAGE to confirm protein composition of the SEC fractions from data shown in D. A_{260}/A_{280} ratios under the lanes were determined by Nanodrop analysis and used to identify fractions containing DNA; n=1.

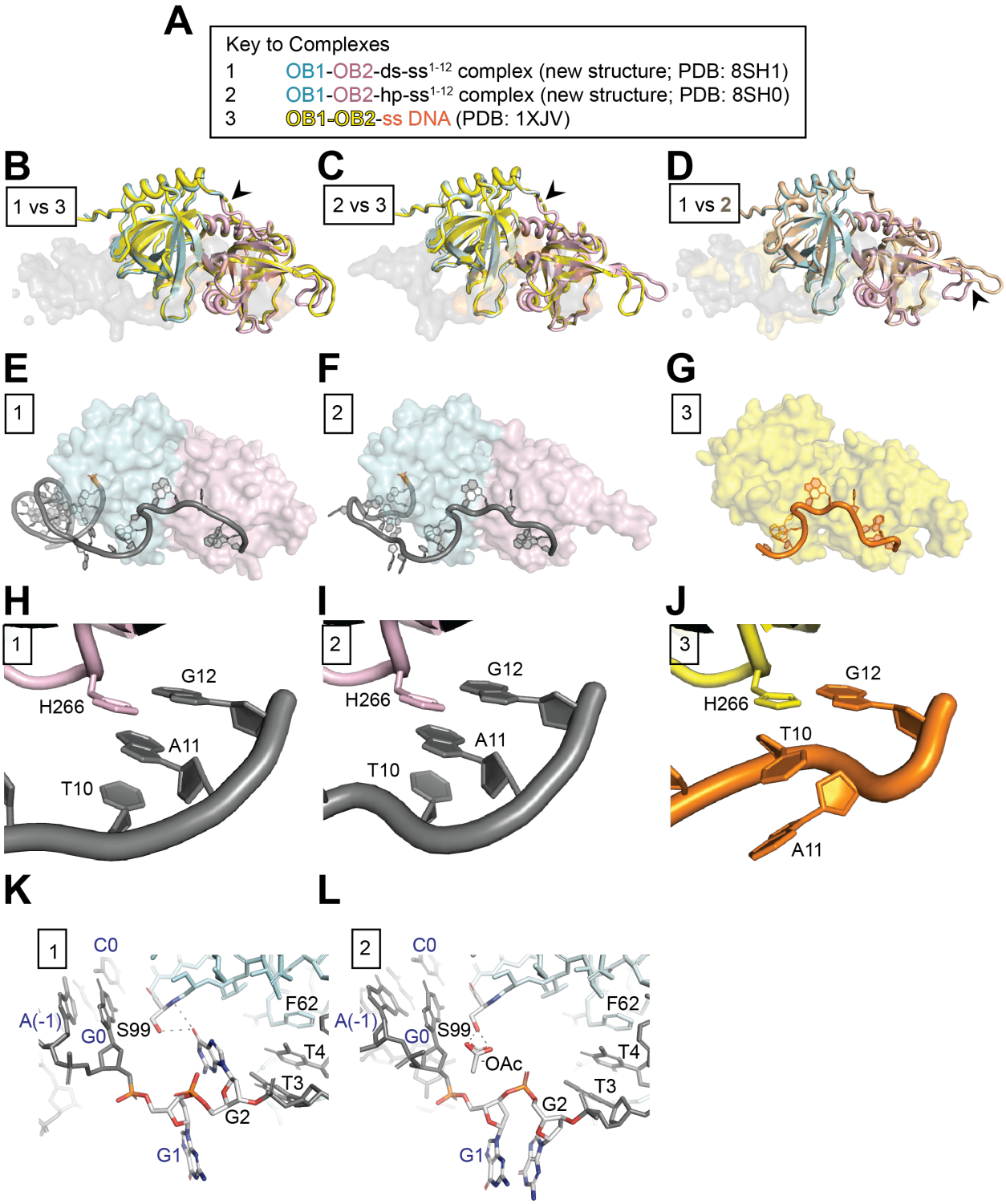

Fig. S3. Comparison of the two structures of hDBD bound to the telomeric ds-ss DNA junction with each other and with the previously solved structure of hDBD-ss DNA. (**A**) Names and color keys for structures shown in all panels except D, where hp-bound hDBD structure is shown in wheat. (**B-G**) Structural comparisons (B-D) or structures (E-G) of indicated complexes. In B-D, the protein is shown in a cartoon representation and the DNA is depicted in a transparent surface representation. In E-G, the DNA is shown in a cartoon representation and the

protein is depicted in a transparent surface representation. hDBD adopts similar conformations in the two new structures (rmsd = 1.0 Å), with the orientation of a POT1 loop (aa 251-258) not involved in DNA binding serving as a notable exception (denoted with the arrowhead in D). hDBD within each new structure is also very similar to hDBD in the ss DNA-bound structure (5'-P-ds-ss$^{1\text{-}12}$ vs. ss DNA-bound hDBD rmsd = 1.5 Å; 5'-P-hp-ss$^{1\text{-}12}$ vs. ss DNA-bound hDBD rmsd = 1.3 Å; A-G). (**H-J**) Both new structures recapitulate the previously reported POT1-ss DNA-binding interface (A-G), barring two differences: the ability to resolve the linker between OB1-OB2 (aa 146-148) in the junction-bound structures (*arrowhead*, B and C), and the stacking orientation of T^{10} and A^{11} with the POT1 H266 sidechain (H-J). (**K** and **L**) Different conformations of G^{2} in the ds versus hp containing DNA-bound structures of hDBD. G^{2} is directed towards OB1 and forms H-bonds with S99 in the hDBD-5'-P-ds-ss$^{1\text{-}12}$ structure (K). This finding is consistent with studies implying enhanced binding of hPOT1 to two full telomeric repeats ^{1}GGTTAGGGTTAG^{12} versus ^{3}TTAGGGTTAG^{12} (*17, 32*). In contrast, in the hDBD-5'-P-hp-ss$^{1\text{-}12}$ structure, G^{2} is flipped out and parallel to G^{1}, likely driven by an ordered acetate anion from the crystallization condition (Material and methods) that H-bonds with the S99 sidechain (L).

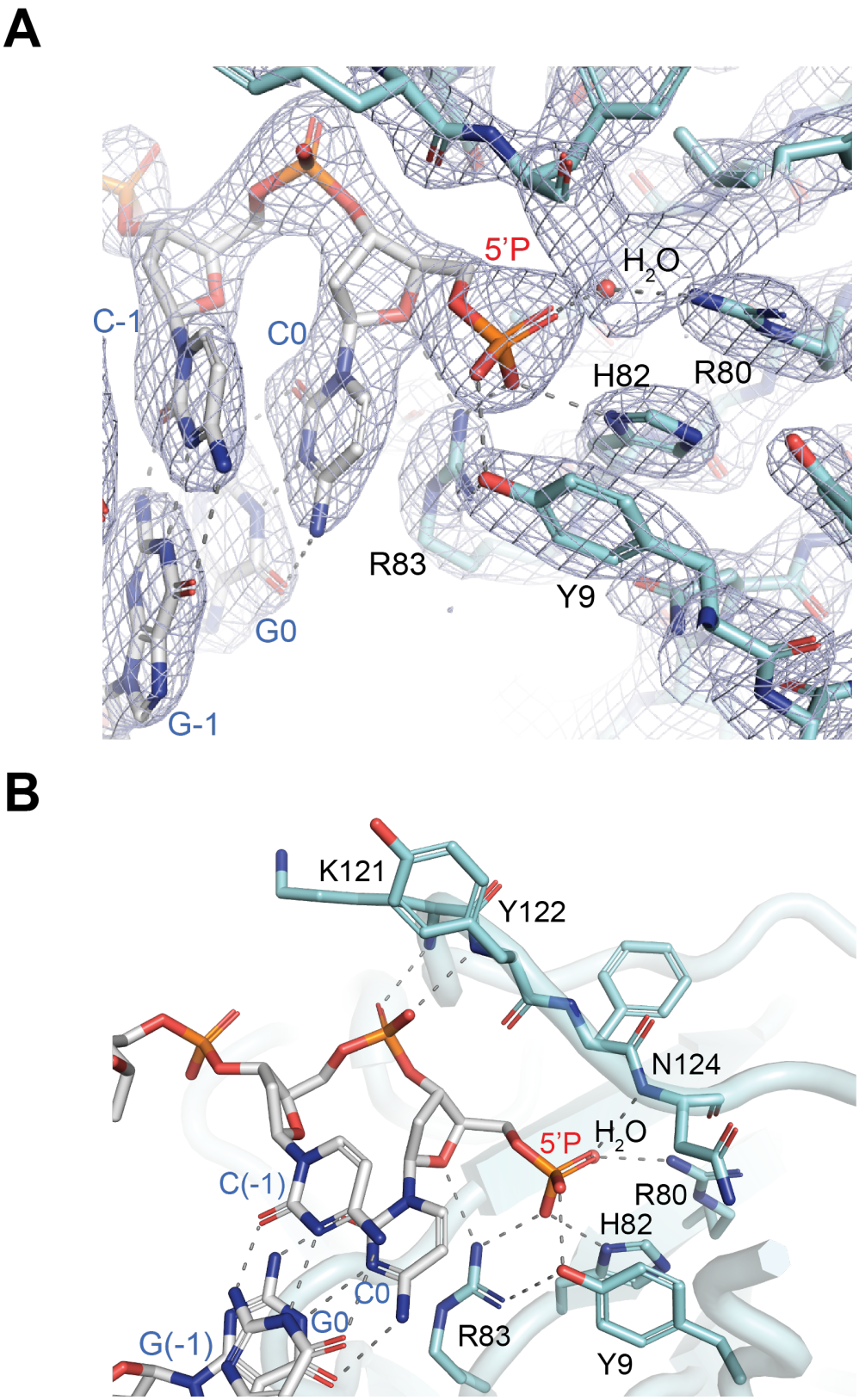

Fig. S4. The structure of the POT-hole-DNA interface. (**A**) $2F_o$-F_c map contoured at 1.5σ for the POT1-DNA junction interface of the structure of hDBD bound to 5'-P-hp-ss$^{1\text{-}12}$. (**B**) Detailed

interactions of the POT1-DNA junction interface, revealing H-bonds between the phosphodiester oxygen atoms on the second nucleotide from the 5'-end and backbone amide atoms of hPOT1 K121, Y122, and N124.

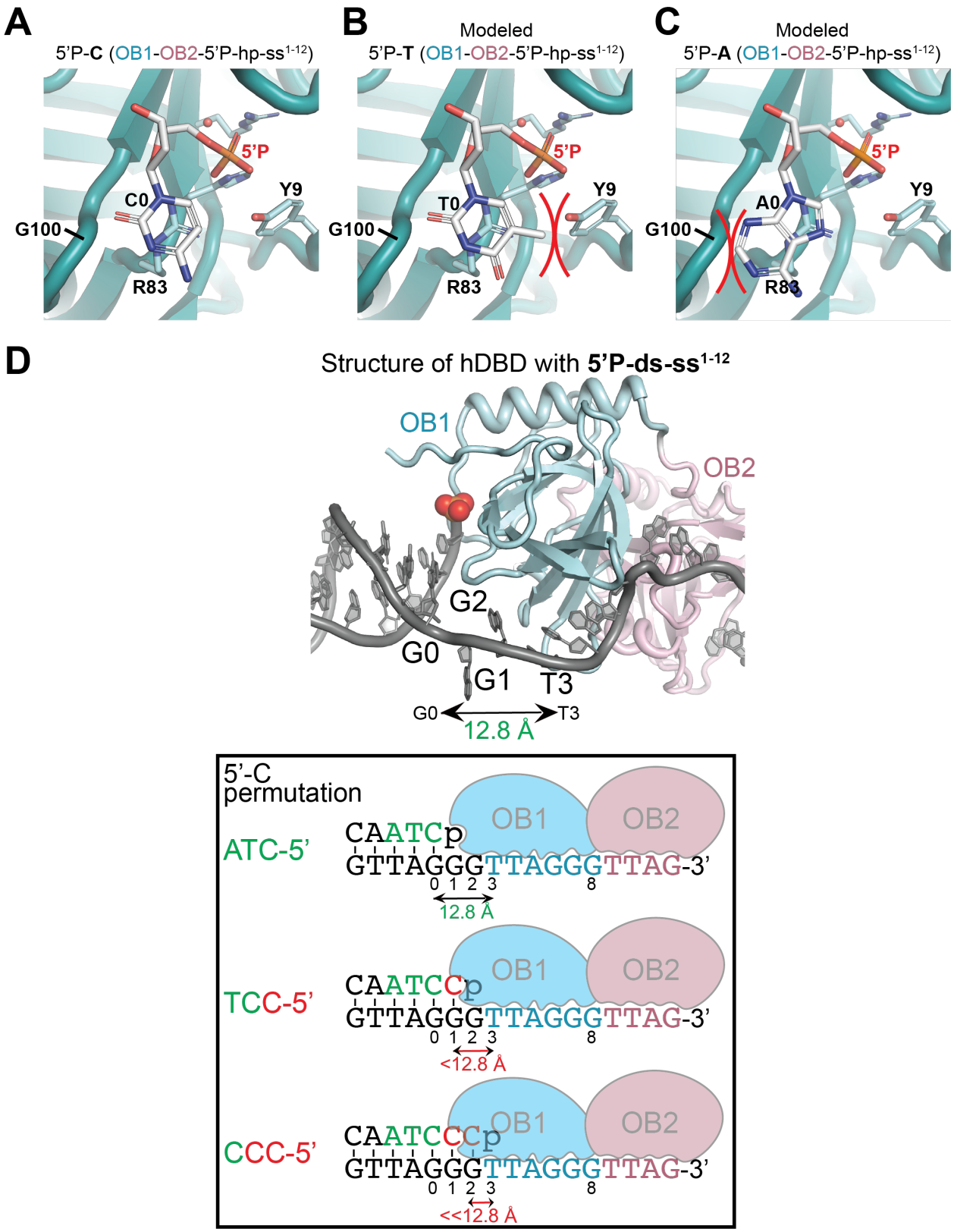

Fig. S5. The POT-hole is specific for a phosphorylated ATC-5'-end at the telomeric ds-ss junction. (**A**) The 5'-phosphorylated C in the POT-hole of hPOT1 fits snugly between the loop containing hPOT1 G100 (left), Y9 (right), and R83 (behind). (**B**) 5'-phosphorylated T modeled

in place of the C suggests a steric clash between the base methyl group and the Y9 sidechain. (**C**) 5'-phosphorylated A modeled in place of the C suggests a steric clash between the bulkier purine ring and the loop containing hPOT1 G100. (**D**) *Top:* The ds-ss DNA junction-bound hDBD structure revealing the distance (12.8 Å) between the POT-hole and the ss DNA binding sites of hPOT1 approximated to be the distance between the junction nucleotide (G0) and the first nucleotide (T3) of the $OB1^{DNA}$ site. *Bottom:* The structure above is schematized, highlighting how the distance between the junction- and ss DNA-binding sites allows a ds-ss junction ending in ATC-5' to simultaneously engage the POT-hole and ss DNA-binding surfaces of hDBD. Specifically, the $^{1}GG^{2}$ dinucleotide between the ds-ss junction and $^{3}TTAGGGTTAG^{12}$ allows the 5'-P end and ss^{3-8} to simultaneously access hPOT1 OB1. Base-pairing of $^{1}GG^{2}$ to the C(s) in the alternative ATC*C*-5' and ATC*CC*-5' configurations would shift the 5' end closer to ss^{3-8}, preventing the two DNA sites from simultaneously engaging hPOT1. For all three 5'-C permutations depicted in the schematic, binding to the ss site is used as an anchor (i.e., unaltered) to assess if the 5'-C can access the POT-hole.

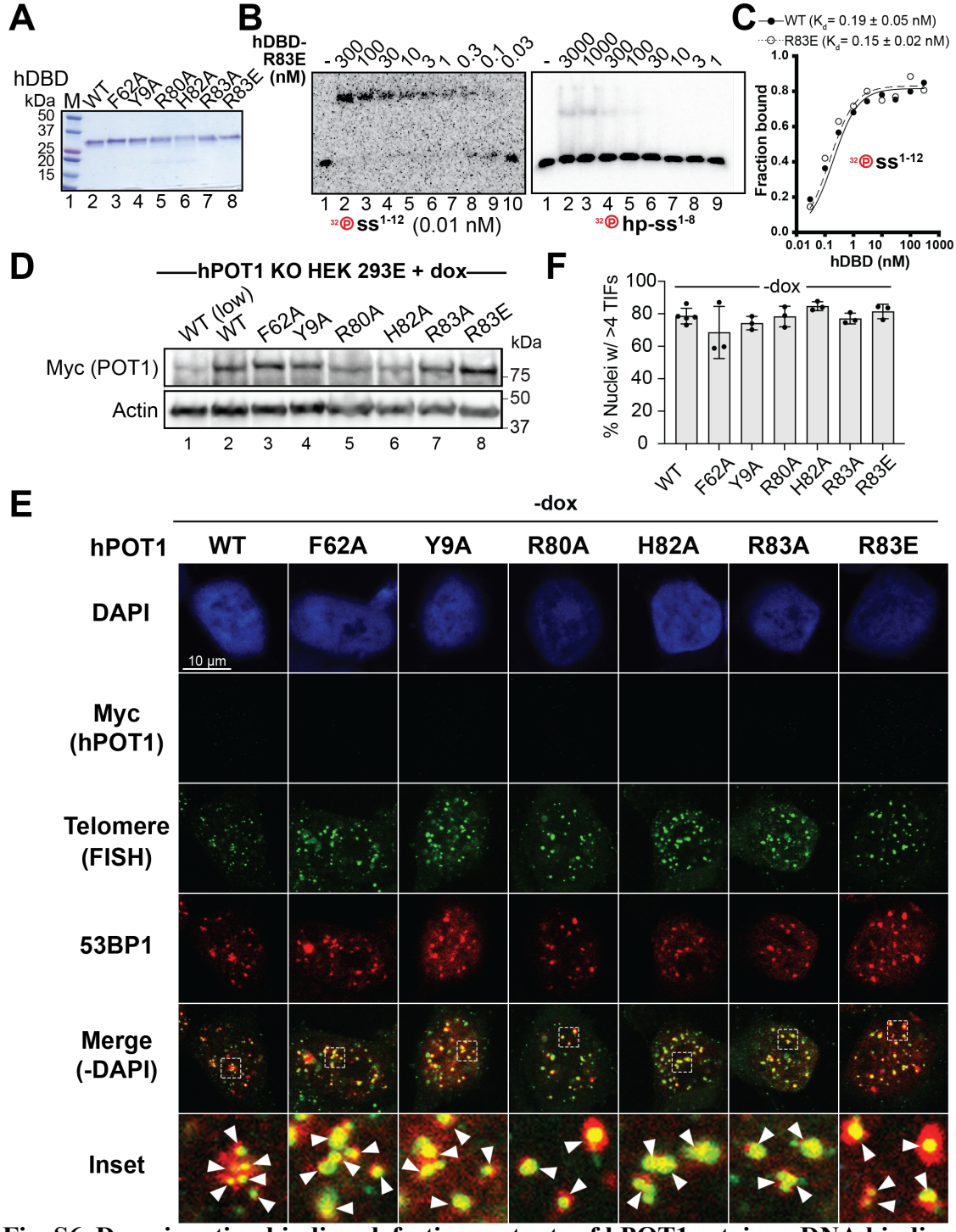

Fig. S6. Ds-ss junction binding-defective mutants of hPOT1 retain ss DNA binding in vitro but result in TIFs at human telomeres. (**A**) Coomassie-stained SDS-PAGE of hDBD WT and mutant protein constructs purified from baculovirus-infected insect cells and used in the EMSA analysis; n=3 (**B**) EMSA analysis of human POT1 DBD R83E POT-hole mutant with 0.01 nM of 5'-P-ss$^{1-12}$ and 0.1 nM of 5'-^{32}P- hp-ss$^{1-8}$; n=3 (**C**) Binding curve of one replicate each of hDBD WT and R83E with 5'-P-ss$^{1-12}$ ss DNA along with K_d and associated SD calculated from n=3

replicates. The WT K_d value is replicated from Fig. 1C. (**D**) Immunoblot of HEK 293E *POT1* KO (induced by 4-OHT) cells complemented with lentivirally-transduced hPOT1-Myc WT and mutant constructs induced with dox. Beta-actin served as a loading control; n=1. (**E**) TIF analysis of cell lines after 4-OHT treatment without supplementation with dox. PNA-FISH was used to detect telomeric DNA (green) and IF was used to detect Myc (hPOT1; cyan) and 53BP1 (red). DAPI was used to stain the nucleus (blue). Overlap of the telomeric and 53BP1 foci in the "Merge" panel (DAPI panel not included) indicates TIFs. Inset shows a magnified view of the boxed area within the image and arrowheads indicate TIFs. The data for WT is replicated from WT (-dox) data in Fig. 3D. (**F**) Quantitation of TIF data of which C is representative. Mean and SD for n=3 sets of images (each set containing >50 nuclei) are plotted for the indicated clonal cell lines.

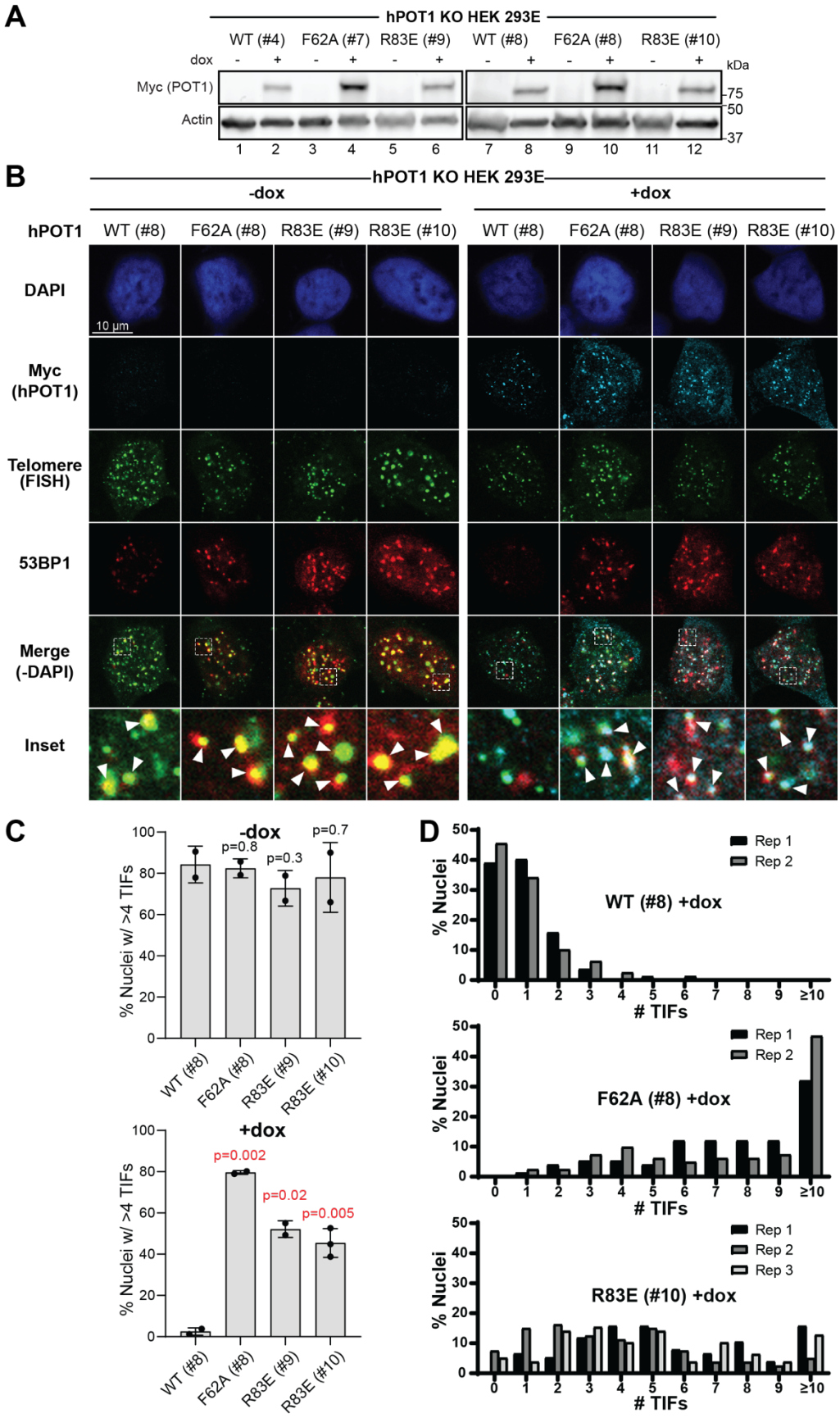
A
hPOT1 KO HEK 293E
WT (#4)
F62A (#7)
R83E (#9)
WT (#8)
F62A (#8)
R83E (#10)
dox
kDa
Myc (POT1)
Actin
75
50
37
1 2 3 4 5 6 7 8 9 10 11 12
B
hPOT1 KO HEK 293E
-dox
+dox
hPOT1
WT (#8)
F62A (#8)
R83E (#9)
R83E (#10)
DAPI
10 µm
Myc (hPOT1)
Telomere (FISH)
53BP1
Merge (-DAPI)
Inset
C
-dox
p=0.8
p=0.3
p=0.7
% Nuclei w/ >4 TIFs
+dox
p=0.002
p=0.02
p=0.005
D
Rep 1
Rep 2
Rep 3
WT (#8) +dox
F62A (#8) +dox
R83E (#10) +dox
% Nuclei
# TIFs
≥10

Fig. S7. Expression and TIF analysis of clonal cell lines expressing ds-ss junction binding-defective mutants of hPOT1. (A) HEK 293E inducible *POT1* KO cells with lentivirally-transduced hPOT1-Myc WT and mutant constructs were used to isolate clones, which were propagated, treated with 4-OHT and either supplemented with dox (1000 ng/ml; "+dox") or not ("-dox") before immunoblotting for Myc (POT1) and beta-actin; n=2. (**B**) TIF analysis of clonal cell lines after 4-OHT and either -dox or +dox (1000 ng/ml) treatment using PNA-FISH for telomeres (green) and IF for Myc (hPOT1; cyan) and 53BP1 (red). DAPI was used to stain the nucleus (blue). Overlap of the telomeric and 53BP1 foci in the "Merge" panel (DAPI panel not included) indicates TIFs. (**C**) Quantitation of TIF data of which B is representative. Mean and SD (n=2 for all conditions except R83E (#10), for which n=3; each set containing >50 nuclei for -dox conditions and >75 nuclei for +dox conditions) for TIFs are plotted for the indicated clonal cell lines. (**D**) Histogram depicting TIF data shown in C (excluding R83E (#9)) plotted as the % of all nuclei analyzed (y-axis) that contain the indicated number of TIFs (x-axis). "Rep" indicates replicate number.

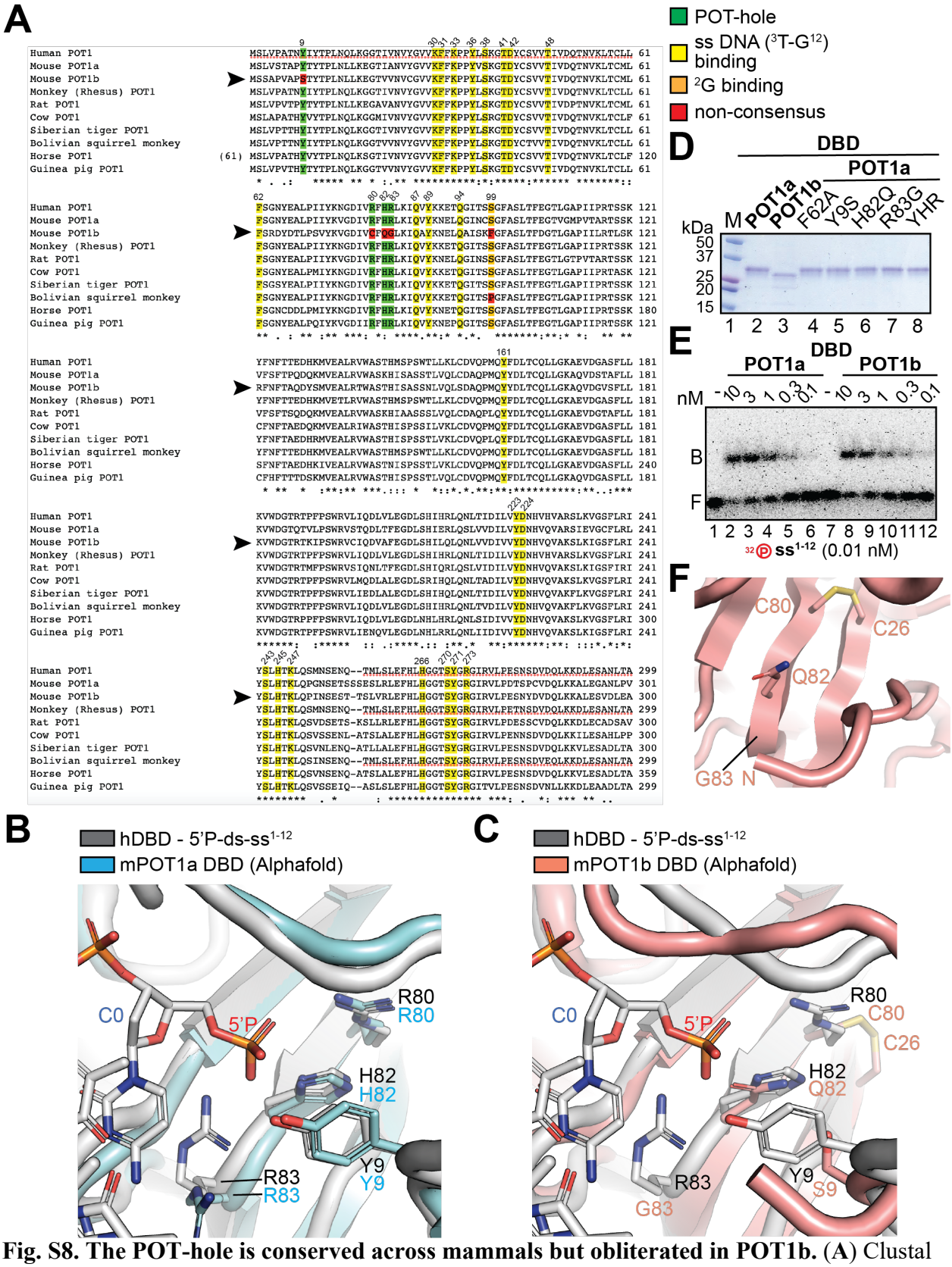

Fig. S8. The POT-hole is conserved across mammals but obliterated in POT1b. (**A**) Clustal Omega-based sequence alignment of DBD (OB1-OB2) from ten mammalian POT1 homologs

including human POT1 and mouse POT1a and POT1b. The color key is shown on the top right. The arrowhead points to the mouse POT1b sequence. The numbering at the top indicates aa numbers for hPOT1. Horse POT1 contains a 60 aa extension at its N-terminus not shown in this alignment. The analysis reveals that the ss DNA-binding residues (yellow) are strictly conserved in POT1b but the POT-hole (green) is completely lost. (**B** and **C**) Alphafold-modeled mouse POT1a DBD (cyan; B) or POT1b DBD (salmon; C) overlaid on hDBD (grey) in the 5'-P-ds-ss$^{1-12}$-bound structure. POT-hole residues in hPOT1 and mouse POT1a as well as residues occupying equivalent positions in the POT1b sequences are shown as sticks. (**D**) Coomassie-stained SDS-PAGE of indicated mouse POT1a and POT1b DBD protein constructs purified after recombinant production in *E. coli* and used in the EMSA analysis; n=3 (**E**) EMSA of DBD constructs of WT mouse POT1a and POT1b with ss$^{1-12}$; DNA at 0.01 nM; n=3. (**F**) Alphafold model predicts a disulfide bridge between POT1b C26 and POT1b C80 (counterpart of POT-hole residue R80 in POT1a) that fortifies the OB1 structure in POT1b. The equivalent of C26 of POT1b is Y26 in POT1a (and hPOT1). We did not examine a POT1a R80C mutation because the resulting surface cysteine would not be capable of forming an equivalent disulfide bridge.

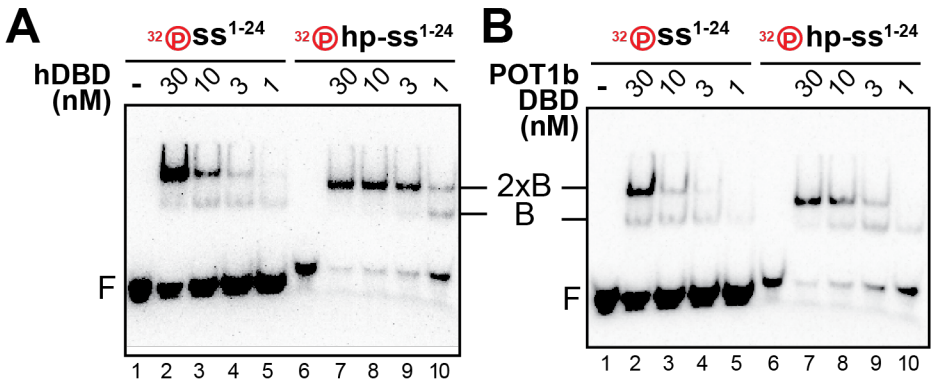

Fig. S9. Protein packing of hPOT1 and mouse POT1b on two DNAs. (**A** and **B**) EMSA analysis demonstrating a discrete high-order complex of hDBD (A) and mouse POT1b DBD (B) with hp-ss$^{1\text{-}24}$ and ss$^{1\text{-}24}$. The data suggest that both proteins can pack in the presence or absence of a ds-ss junction. Our structural and biochemical data and previous studies are consistent with hDBD harboring both ds-ss junction and TTAG-3' end-binding preferences, and POT1b exhibiting only a TTAG-3'end-binding preference. However, additional analysis is required to unequivocally determine the 3'-end-binding preference of these proteins. DNA at 0.1 nM; n=3.

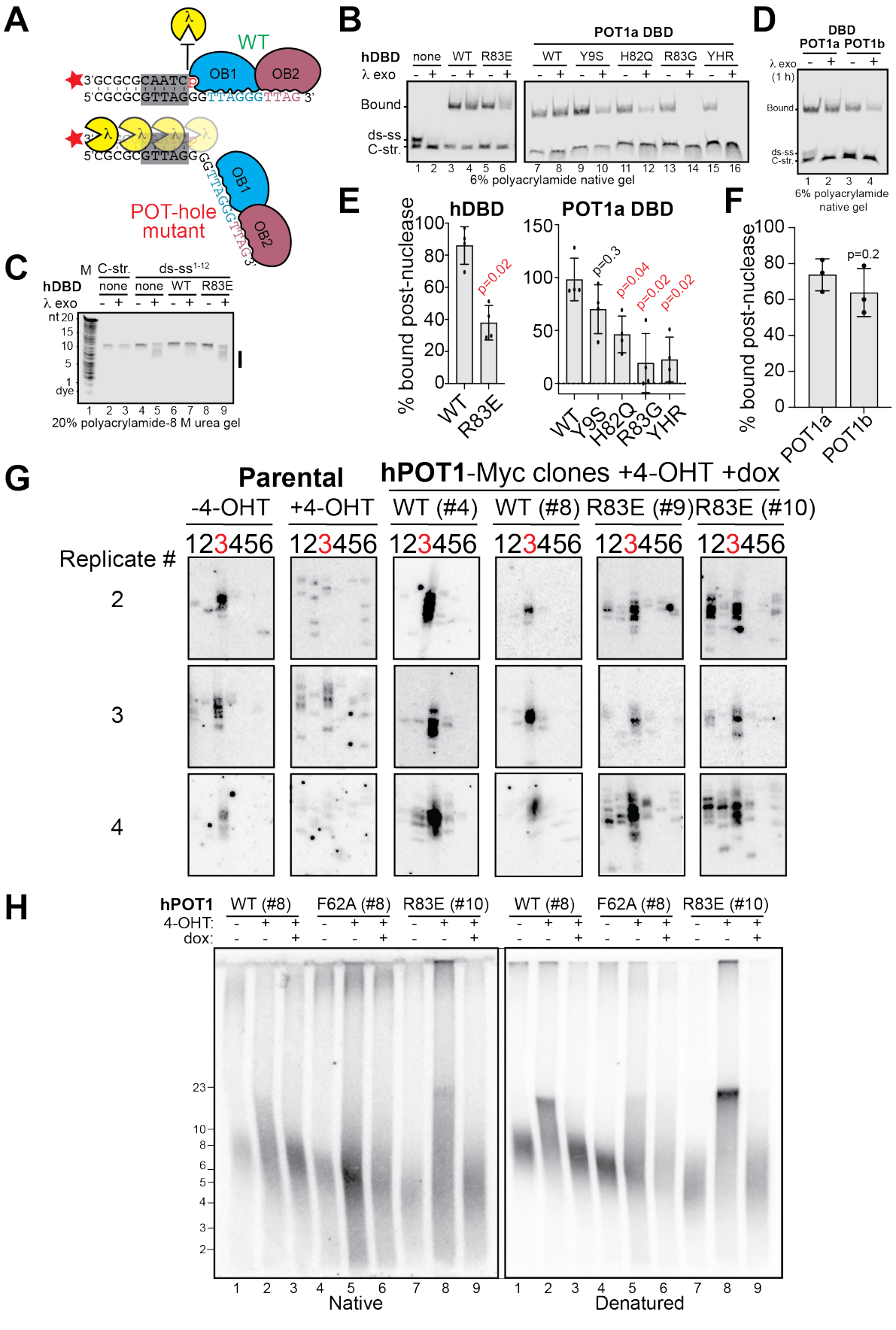
A
WT
OB1
OB2
3'GCGCGCAATC
5'CGCGCGTTAGGGTTAGGGTTAG 3'
POT-hole mutant
B
POT1a DBD
hDBD none WT R83E WT Y9S H82Q R83G YHR
λ exo
Bound
ds-ss
C-str.
6% polyacrylamide native gel
D
DBD
POT1a POT1b
λ exo (1 h)
Bound
ds-ss
C-str.
6% polyacrylamide native gel
C
M C-str. ds-ss1-12
hDBD none none WT R83E
λ exo
nt 20 15 10 5 1 dye
I
20% polyacrylamide-8 M urea gel
E
hDBD
POT1a DBD
% bound post-nuclease
p=0.02
p=0.3
p=0.04
p=0.02
p=0.02
WT R83E
WT Y9S H82Q R83G YHR
F
% bound post-nuclease
p=0.2
POT1a POT1b
G
Parental
hPOT1-Myc clones +4-OHT +dox
-4-OHT +4-OHT WT (#4) WT (#8) R83E (#9) R83E (#10)
Replicate #
2
3
4
H
hPOT1 WT (#8) F62A (#8) R83E (#10) WT (#8) F62A (#8) R83E (#10)
4-OHT:
dox:
23 10 8 6 5 4 3 2
Native
Denatured

Fig. S10. The POT-hole defines the 5' end of human chromosomes. (**A**) Schematic of λ-exonuclease-protection assay to measure the protection of the 5' nt at the ds-ss junction by DBD constructs. The DNA duplex used is the same as that used in crystallography (5'-P-ds-ss$^{1\text{-}12}$) except that the 3' end of the C-strand was labeled with a fluorophore (IRDye 800CW). WT POT1 DBD is expected to protect against exonucleolytic degradation whereas incubation with POT1-hole mutants (or absence of any DBD) would result in the degradation of the 5'-P-containing C-strand until it is too short to base pair with its complement or be further degraded by λ-exonuclease. (**B**) 5'-end-protection assay with fluorophore-labeled 5'-P-ds-ss$^{1\text{-}12}$ (10 nM) and indicated human and mouse POT1a DBD (50 nM) constructs treated with 0.4 units of λ-exonuclease for 10 min at room temperature before EMSA analysis. The free DNA resolves into two bands: the top and bottom bands for free DNA represent the ds-ss$^{1\text{-}12}$ and excess of the 5'-P-containing C-strand, respectively. The binding of DBD protein constructs to ds-ss$^{1\text{-}12}$ results in a slower-migrating complex at the expense of the free ds-ss$^{1\text{-}12}$ DNA. Degradation of the 5'-P-containing C-strand, as observed with complexes with POT-hole mutants or the absence of DBD, results in the loss of the signal for the slower-migrating band; n=4. (**C**) Analysis of the λ-exonuclease protection assay samples on a denaturing gel. Note that only the labeled C-rich strand of the duplex is visualized. λ-exonuclease is inefficient at processing a ss DNA substrate ("C-str", which is the C-rich strand alone) under the conditions of this experiment. The vertical bar indicates λ-exonuclease degradation products of the C-strand within ds-ss$^{1\text{-}12}$. "M" indicates an RNA hydrolysis ladder of indicated size markers; n=3. (**D**) Despite lacking a POT-hole, POT1b DBD moderately protected 5'-P-ds-ss$^{1\text{-}12}$ from λ-exonuclease even under the 1 h digestion condition used here; n=3. Although the mechanism is unclear, it is worth noting that POT1b it is better able to complement a *POT1a* KO when its interaction with the CST complex is compromised (i.e., it is relieved of one of its 3'-end replication functions) (*16*). (**E** and **F**) Mean and SD for data of which B (for E; n=4) and D (for F; n=3) are representative. P-values calculated using a two-tailed Student's t-test for comparisons against WT data (E) or POT1a (F) are indicated above the bars. (**G**) Remaining three replicates of STELA-based determination of the chromosomal 5'-terminal nucleotide used to generate the quantitation shown in Fig. 5C. (**H**) *Left:* Telomere restriction fragment (TRF) analysis of indicated clonal cell lines performed first under native conditions with a 5'-^{32}P-labeled telomeric C-probe $(CTAACC)_4$ to detect the ss G-rich overhang signal. *Right:* Telomere restriction fragment (TRF) analysis after denaturing the DNA on the same gel and re-probing it (with the same probe) to detect the total telomeric DNA signal; n=1.

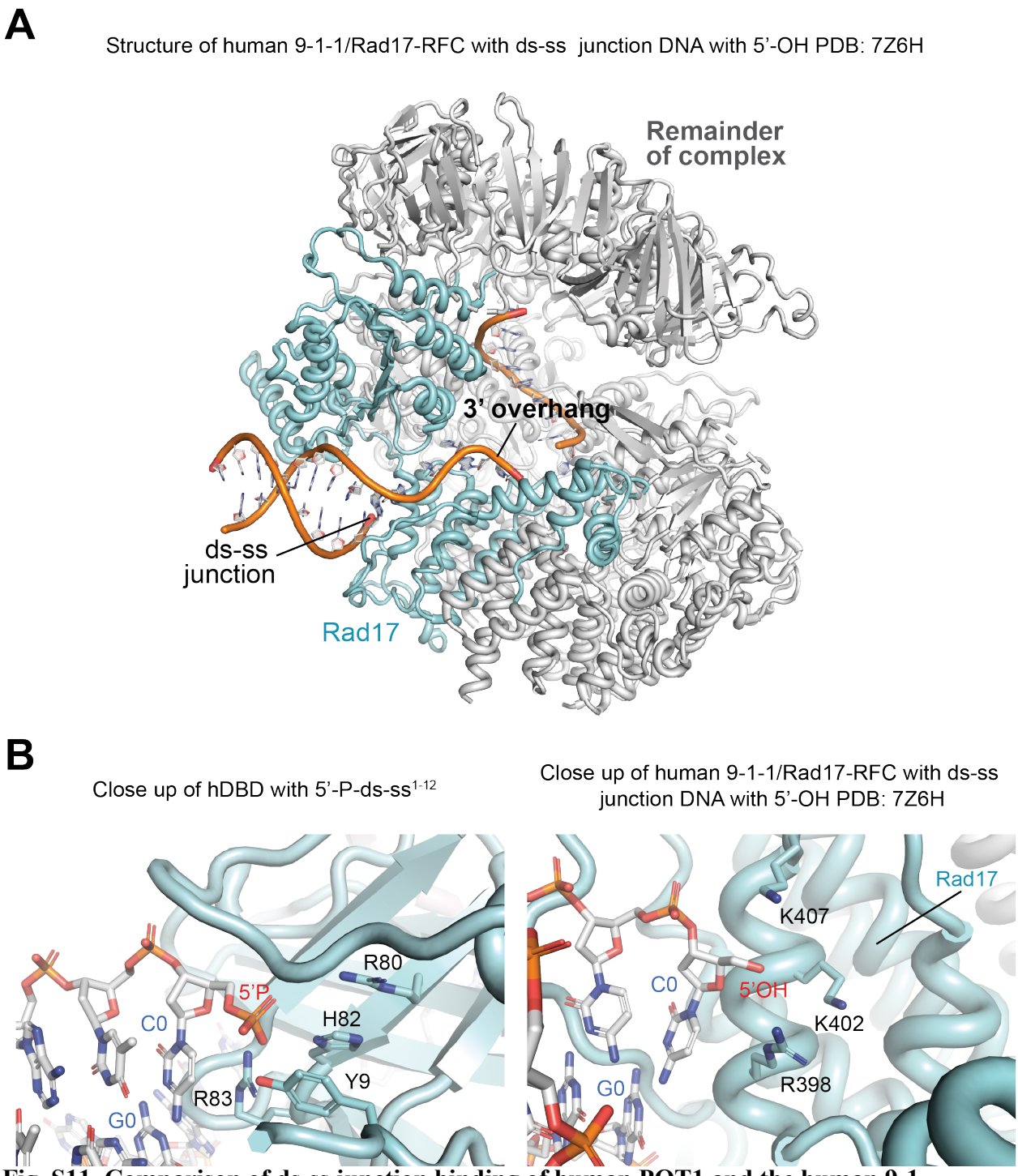

Fig. S11. Comparison of ds-ss junction binding of human POT1 and the human 9-1-1/Rad17-RFC complex involved in ATR signaling. (**A**) Cartoon representation of the ds-ss DNA junction-bound human 9-1-1/Rad17-RFC complex (PDB: 7Z6H). The structure shows how Rad17 (blue) binds the ds-ss junction, including the 5'-end and a short stretch of the ss overhang. The remainder of the complex, including 9-1-1 and the RFC subunits, are shown in grey. (**B**) Side-by-side comparisons of the ds-ss junction-bound structures of hDBD and 9-1-1/Rad17-RFC (PDB: 7Z6H). In the latter structure, the 5'-OH at the junction (the DNA used did not contain a

5’-P) occupies an electropositive pocket consisting of lysine and arginine residues, similar to the 5’-P end protection mechanism of the hPOT1 POT-hole.

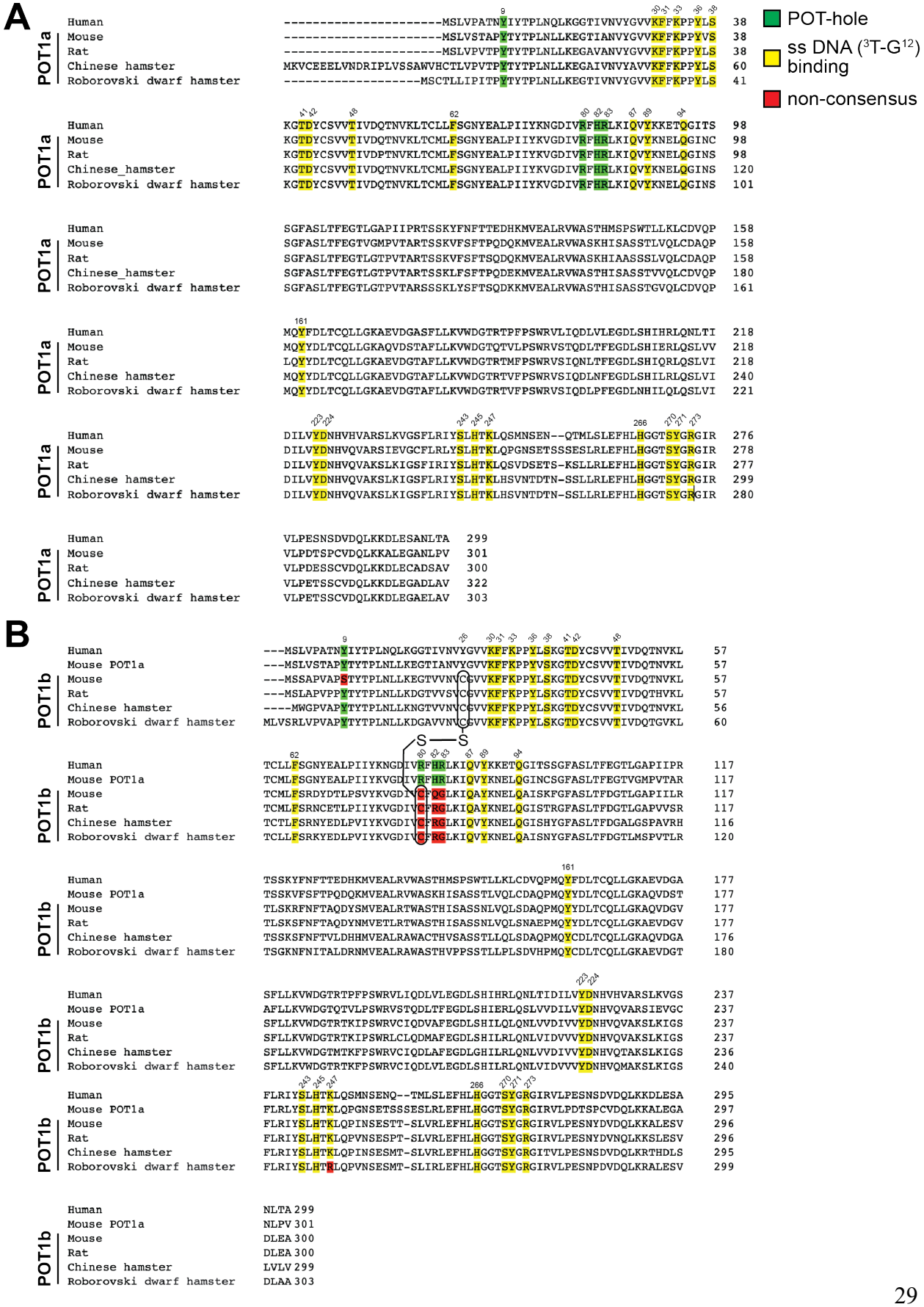
A
POT1a
Human
Mouse
Rat
Chinese hamster
Roborovski dwarf hamster
POT-hole
ss DNA (^{3}T-G^{12}) binding
non-consensus
B
POT1b
Human
Mouse POT1a
Mouse
Rat
Chinese hamster
Roborovski dwarf hamster
S—S

Fig. S12. In families of the Rodentia order, the ss DNA-binding residues are conserved in both POT1 paralogs but the POT-hole is lost in POT1b. Clustal Omega-based sequence alignment of DBD (OB1-OB2) of hPOT1, mouse POT1a, and either other POT1a homologs (**A**) or POT1b homologs (**B**) from the indicated rodents. The color key is shown on the top right of A. The numbering at the top indicates aa numbers for hPOT1. Mouse POT1b C80 and its disulfide partner C26 are conserved among POT1b homologs, suggesting conservation of the disulfide bridge (indicated by -S-S-).

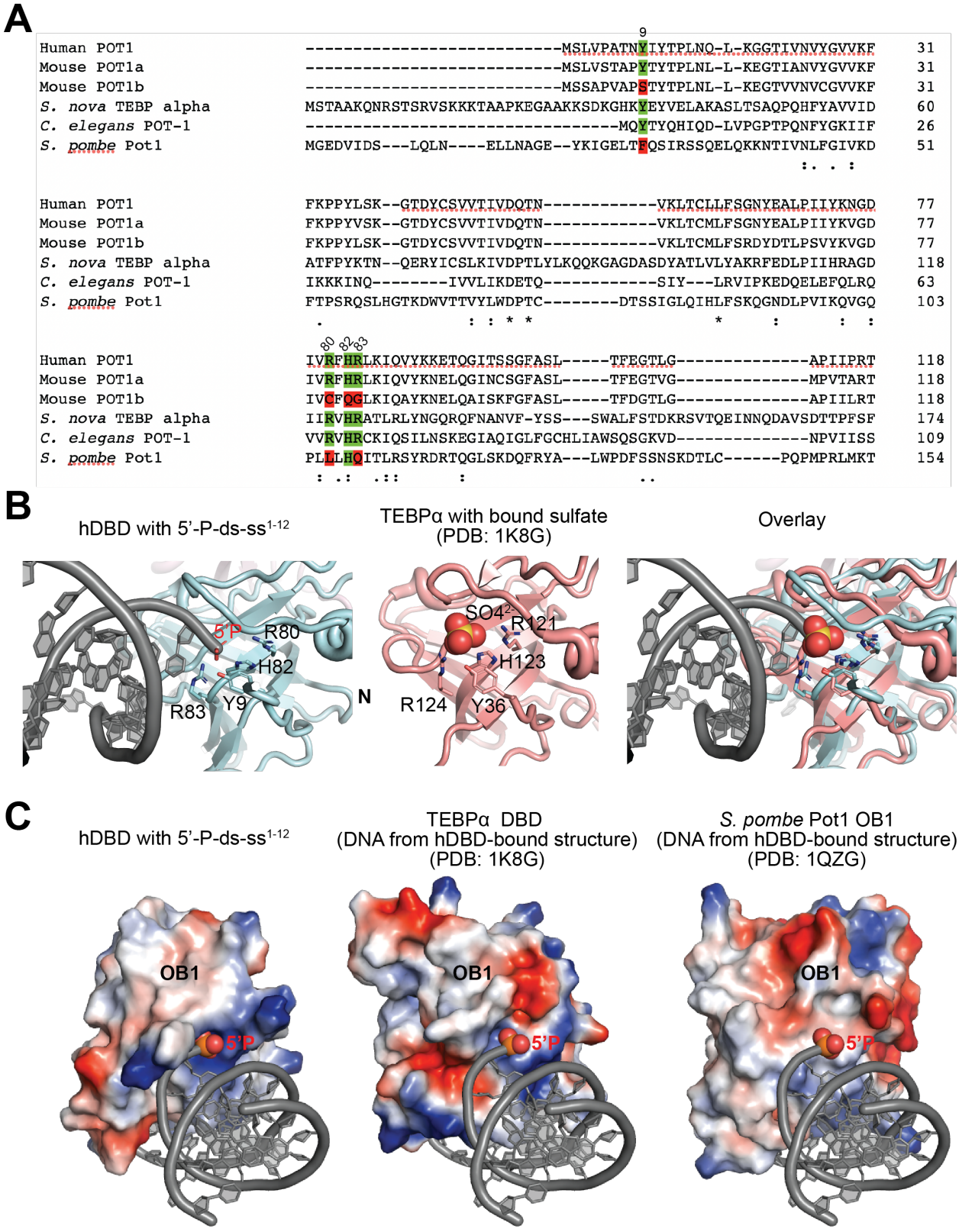

Fig. S13. POT-hole analysis in diverse eukaryotic POT1 homologs. (**A**) Sequence analysis of POT1 homologs from indicated species to show conservation of POT-hole (in green) or lack thereof (in red). The numbering at the top indicates aa numbers for hPOT1. (**B**) Ds-ss junction-

bound hDBD structure (*left*), published sulfate-bound *S. nova* TEBPα structure (*center*), and their overlay (*right*) demonstrating that the sulfate ion and 5'-P are superimposable. (**C**) Electrostatic surface representations of the ds-ss junction-bound hDBD OB1 and OB1 from indicated POT1 homologs aligned to it. The ds-ss$^{1\text{-}8}$ DNA from the hDBD-bound structure is included in each view to locate the putative POT-hole (by proximity to the 5'-P shown as atomic spheres). ss$^{9\text{-}12}$ (OB2^{DNA}) is omitted from the structural representation for clarity. An electropositive surface consistent with a POT-hole is obvious for TEBPα, but not *S. pombe* Pot1.

Table S1: Data collection and refinement statistics for 5'-phosphorylated ds-ss junction DNA-bound hDBD structures.

	Structure of human POT1 DBD w 5'-P-hp-ss$^{1-12}$ (PDB: 8SH0)	Structure of human POT1 DBD 5'-P-ds-ss$^{1-12}$ (PDB: 8SH1)
Data collection		
Space group	P 32 2 1	I 2 2 2
Cell dimensions		
a, *b*, *c* (Å)	67.230 67.230 143.373	58.470 170.620 173.960
α, β, γ (°)	90 90 120	90.00 90.00 90.00
Wavelength (Å)	1.12723	1.12713
Resolution (Å)	71.69 - 2.16 (2.23 - 2.16)	86.98 – 2.60 (2.72 – 2.60)
R_{merge}	0.086 (1.131)	0.146 (7.070)
$CC_{1/2}$	0.999 (0.858)	0.997 (0.270)
$I / \sigma I$	19.6 (3.4)	10.2 (0.5)
Overall Completeness (%)	100 (100.00)	99.7 (99.9)
Redundancy	19.3 (20.4)	13.4 (14.0)
Refinement		
Resolution (Å)	45.19 - 2.16 (2.22 - 2.16)	42.66 – 2.60 (2.65 – 2.60)
No. reflections	38944 (3088)	50917 (2502)
R_{work} / R_{free}	0.1800/0.2214 (0.2492/0.2898)	0.2303/0.2544 (0.5509/0.5670)
No. atoms	2891	3042
Protein	2339	2333
DNA	420	664
Ligand	12 (Acetate)	0
Water	120	45
B-factors	63.64	128.89
Protein	61.62	113.72
DNA	75.70	183.71
Water	58.88	106.1
R.m.s deviations		
Bond lengths (Å)	0.003	0.003
Bond angles (°)	0.646	0.590
Ramachandran favored (%)	97.60	96.22
Ramachandran allowed (%)	2.05	3.78
Ramachandran outliers (%)	0.34 (Val174)	0
Molprobity overall score	1.26	1.60
Molprobity percentile (%)	100	99

Table S2: Details of synthetic oligonucleotides used in the study.

Oligonucleotide name	Sequence (5' to 3')	Purpose	New/Published
ss^{1-12}	GGTTAGGGTTAG	EMSA	(*55*)
hp-ss^{1-8}	CCAGCAGGGGTTAGGG	EMSA	New
5'-P-hp-ss^{1-8}	Phosph/CCAGCAGGGGTTAGGG	EMSA	New
no_ hp-ss^{1-8}	AAAGCAAAGGTTAG	EMSA	New
hp-ss^{1-12}	CCAGCAGGGGTTAGGGTTAG	EMSA	New
long_ds-ss^{1-8} G-rich strand	GGATGTCACTCAGCAGACGGGAATTCGTAAGTTAGGGTTAGGG	EMSA	New, non-telomeric ds region adapted from (*17*)
long_ds-ss^{1-8} C-rich strand	CTAACTTACGAATTCCCGTCTGCTGAGTGACATCC	EMSA	New, non-telomeric ds region adapted from (*17*)
ss^{1-24}	GGTTAGGGTTAGGGTTAGGGTTAG	EMSA	New
hp-ss^{1-24}	CCAGCAGGGGTTAGGGTTAGGGTTAGGGTTAG	EMSA	New
5'-P-hp-ss^{1-12}	Phosph/CCAGCAGGGGTTAGGGTTAG	Crystallography	New
Anchor(10ds)ss^{1-12}	CGCGCGTTAGGGTTAGGGTTAG	Crystallography and exonuclease assay	New
5'-P-Anchor(10ds)-C_strand	Phosph/CTAACGCGCG	Crystallography	New

5'-P-Anchor(10ds)-C_strand/IRDye 800CW	Phosph/CTAACGCGCG/IRDye 800CW	Exonuclease assay	New
XpYpE2 (forward primer subtelomeric):	TTGTCTCAGGGTCCTAGTG	STELA	(*23*)
XpYpB2 (reverse primer subtlelomeric):	TCTGAAAGTGGACC(A/T)ATCAG	STELA	(*23*)
C-telorette 1	TGCTCCGTGCATCTGGCATCCCCTAAC	STELA	(*23*)
C-telorette 2	TGCTCCGTGCATCTGGCATCTAACCCT	STELA	(*23*)
C-telorette 3	TGCTCCGTGCATCTGGCATCCCTAACC	STELA	(*23*)
C-telorette 4	TGCTCCGTGCATCTGGCATCCTAACCC	STELA	(*23*)
C-telorette 5	TGCTCCGTGCATCTGGCATCAACCCTA	STELA	(*23*)
C-telorette 6	TGCTCCGTGCATCTGGCATCACCCTAA	STELA	(*23*)
C-teltail (reverse primer):	TGCTCCGTGCATCTGGCATC	STELA	(*23*)
hY9A-F	CTTTGGTTCCAGCAACAAATgcTATATATACACCCCTGAATCAACTT	hPOT1 mutagenesis	New
hY9A-R	AAGTTGATTCAGGGGTGTATATATAgcATTTGTTGCTGGAACCAAAG	hPOT1 mutagenesis	New

hR80A-F	CCAATAATTTATAAAAATGGAGATATTGTTgcCTTTCACAGGCTGAAGATTCA	hPOT1 mutagenesis	New
hR80A-R	TGAATCTTCAGCCTGTGAAAGgcAACAATATCTCCATTTTTATAAATTATTGG	hPOT1 mutagenesis	New
hH82A-F	TATAAAAATGGAGATATTGTTCGCTTTgcCAGGCTGAAGATTCAAGTATATAAAAAG	hPOT1 mutagenesis	New
hH82A-R	CTTTTTATATACTTGAATCTTCAGCCTGgcAAAGCGAACAATATCTCCATTTTTATA	hPOT1 mutagenesis	New
hR83A-F	GGAGATATTGTTCGCTTTCACgcGCTGAAGATTCAAGTATATAAAAAGGAG	hPOT1 mutagenesis	New
hR83A-R	CTCCTTTTTATATACTTGAATCTTCAGCgcGTGAAAGCGAACAATATCTCC	hPOT1 mutagenesis	New
hR83E-F	GGAGATATTGTTCGCTTTCACgaGCTGAAGATTCAAGTATATAAAAAGGAG	hPOT1 mutagenesis	New
hR83E-R	CTCCTTTTTATATACTTGAATCTTCAGCtcGTGAAAGCGAACAATATCTCC	hPOT1 mutagenesis	New
hF62A-F	GTAAAACTAACTTGCCTGCTCgcTAGTGGAAACTATGAAGCCC	hPOT1 mutagenesis	New
hF62A-R	GGGCTTCATAGTTTCCACTAgcGAGCAGGCAAGTTAGTTTTAC	hPOT1 mutagenesis	New
pcDNA-hPOT1-HpaF	agatGTTAACGCCGCcaccATGTCTTTGG	hPOT1 cloning into lentiviral vector	New

pcDNA-hPOT1Myc-PacI-R	agatTTAATTAAGTAGTCCTCGACCTAGAGATCTTCTTCG	hPOT1 cloning into lentiviral vector	New
hPOT1-650R	AGGCTATAGATTCTAAGAAAGC	hPOT1 sequencing primer	New
hPOT1-650F	CACCAGGACACCATTTCC	hPOT1 sequencing primer	New
hPOT1-1300F	CTAAAACCCCAGTTGTCAAG	hPOT1 sequencing primer	New
mpta-f	ATTGGTGGATCCATGTCTTTGGTTTCAACAGC	Mouse POT1a DBD cloning	(*55*)
mpta-xho-v301r	AGTTGACTCGAGTTAGACTGGCAAATTTGCACCTTC	Mouse POT1a DBD cloning	(*55*)
mA-Y9S-F	ctttggtttcaacagctcccagtacatatacacccctgaatc	Mouse POT1a DBD mutagenesis	New
mA-Y9S-R	gattcaggggtgtatatgtactgggagctgttgaaaccaaag	Mouse POT1a DBD mutagenesis	New
mA-H82Q-F	tggagacattgttcgcttccagaggctgaagatc	Mouse POT1a DBD mutagenesis	New
mA-H82Q-R	gatcttcagcctctggaagcgaacaatgtctcca	Mouse POT1a DBD mutagenesis	New
mA-R83G-F	acattgttcgcttccacgggctgaagatccaagtg	Mouse POT1a DBD mutagenesis	New

mA-R83G-R	cacttggatcttcagcccgtggaagcgaacaatgt	Mouse POT1a DBD mutagenesis	New
mA-F62A-F	gtgaagttaacctgtatgctcgctagtggaaactatgaagccct	Mouse POT1a DBD mutagenesis	New
mA-F62A-R	agggcttcatagtttccactagcgagcatacaggttaacttcac	Mouse POT1a DBD mutagenesis	New
mptb-f	ATTGGTGGATCCATGTCTTCGGCCCCAGTAGC	Mouse POT1b DBD cloning	New
mptb-xho-a300r	TCATCTGACTCGAGTTAGGCTTCCAAGTCTACAGATTC	Mouse POT1b DBD cloning	New
mmPot1a-500-F	TGACCTGTCAGCTCCTGGGTAAAGC	Mouse POT1a sequencing	(*55*)
mmPot1a-1000-F	ATCACCTTATGAAGAAGAACGATGTC	Mouse POT1a sequencing	(*55*)
mmPot1a-1500-F	CCTTACCCTTTCAGCCCCGTTCCTC	Mouse POT1a sequencing	(*55*)
mmPot1b-500-F	GTGCAGCTTTCTGATGCTCAGCCC	Mouse POT1b sequencing	New
mmPot1b-1000-F	CATCTTCAAGCTCCGAATCAGACC	Mouse POT1b sequencing	New
mmPot1b-1500-F	GTCACTATGGATGTAAACAGTGCTC	Mouse POT1b sequencing	New
TelC-Cy3 PNA FISH probe:	Cy3-CCCTAACCCTAACCCTAA (This is a synthetic PNA)	Telomere FISH probe	PNA Bio; F1002

Telomeric C-probe	CTAACCCTAACCCTAACCCTAACC	TRF analysis	New

References and Notes

1. W. Palm, T. de Lange, How shelterin protects mammalian telomeres. *Annu. Rev. Genet.* **42**, 301–334 (2008).

2. E. L. Denchi, T. de Lange, Protection of telomeres through independent control of ATM and ATR by TRF2 and POT1. *Nature* **448**, 1068–1071 (2007).

3. T. de Lange, Shelterin-Mediated Telomere Protection. *Annu. Rev. Genet.* **52**, 223–247 (2018).

4. J. C. Saldivar, D. Cortez, K. A. Cimprich, The essential kinase ATR: Ensuring faithful duplication of a challenging genome. *Nat. Rev. Mol. Cell Biol.* **18**, 622–636 (2017).

5. P. Baumann, T. R. Cech, Pot1, the putative telomere end-binding protein in fission yeast and humans. *Science* **292**, 1171–1175 (2001).

6. Y. Gong, T. de Lange, A Shld1-controlled POT1a provides support for repression of ATR signaling at telomeres through RPA exclusion. *Mol. Cell* **40**, 377–387 (2010).

7. M. Lei, E. R. Podell, T. R. Cech, Structure of human POT1 bound to telomeric single-stranded DNA provides a model for chromosome end-protection. *Nat. Struct. Mol. Biol.* **11**, 1223–1229 (2004).

8. D. E. Gottschling, V. A. Zakian, Telomere proteins: Specific recognition and protection of the natural termini of Oxytricha macronuclear DNA. *Cell* **47**, 195–205 (1986).

9. C. M. Price, T. R. Cech, Telomeric DNA-protein interactions of Oxytricha macronuclear DNA. *Genes Dev.* **1**, 783–793 (1987).

10. M. P. Horvath, V. L. Schweiker, J. M. Bevilacqua, J. A. Ruggles, S. C. Schultz, Crystal structure of the Oxytricha nova telomere end binding protein complexed with single strand DNA. *Cell* **95**, 963–974 (1998).

11. C. I. Nugent, T. R. Hughes, N. F. Lue, V. Lundblad, Cdc13p: A single-strand telomeric DNA-binding protein with a dual role in yeast telomere maintenance. *Science* **274**, 249–252 (1996).

12. J. J. Lin, V. A. Zakian, The Saccharomyces CDC13 protein is a single-strand TG1-3 telomeric DNA-binding protein in vitro that affects telomere behavior in vivo. *Proc. Natl. Acad. Sci. U.S.A.* **93**, 13760–13765 (1996).

13. M. Raices, R. E. Verdun, S. A. Compton, C. I. Haggblom, J. D. Griffith, A. Dillin, J. Karlseder, C. elegans telomeres contain G-strand and C-strand overhangs that are bound by distinct proteins. *Cell* **132**, 745–757 (2008).

14. L. Wu, A. S. Multani, H. He, W. Cosme-Blanco, Y. Deng, J. M. Deng, O. Bachilo, S. Pathak, H. Tahara, S. M. Bailey, Y. Deng, R. R. Behringer, S. Chang, Pot1 deficiency initiates DNA damage checkpoint activation and aberrant homologous recombination at telomeres. *Cell* **126**, 49–62 (2006).

15. D. Hockemeyer, J. P. Daniels, H. Takai, T. de Lange, Recent expansion of the telomeric complex in rodents: Two distinct POT1 proteins protect mouse telomeres. *Cell* **126**, 63–77 (2006).

16. K. Kratz, T. de Lange, Protection of telomeres 1 proteins POT1a and POT1b can repress ATR signaling by RPA exclusion, but binding to CST limits ATR repression by POT1b. *J. Biol. Chem.* **293**, 14384–14392 (2018).

17. W. Palm, D. Hockemeyer, T. Kibe, T. de Lange, Functional dissection of human and mouse POT1 proteins. *Mol. Cell. Biol.* **29**, 471–482 (2009).

18. P. Gu, S. Jia, T. Takasugi, V. M. Tesmer, J. Nandakumar, Y. Chen, S. Chang, Distinct functions of POT1 proteins contribute to the regulation of telomerase recruitment to telomeres. *Nat. Commun.* **12**, 5514 (2021).

19. L. Y. Chen, S. Redon, J. Lingner, The human CST complex is a terminator of telomerase activity. *Nature* **488**, 540–544 (2012).

20. P. Wu, H. Takai, T. de Lange, Telomeric 3′ overhangs derive from resection by Exo1 and Apollo and fill-in by POT1b-associated CST. *Cell* **150**, 39–52 (2012).

21. M. Wan, J. Qin, Z. Songyang, D. Liu, OB fold-containing protein 1 (OBFC1), a human homolog of yeast Stn1, associates with TPP1 and is implicated in telomere length regulation. *J. Biol. Chem.* **284**, 26725–26731 (2009).

22. D. Hockemeyer, A. J. Sfeir, J. W. Shay, W. E. Wright, T. de Lange, POT1 protects telomeres from a transient DNA damage response and determines how human chromosomes end. *EMBO J.* **24**, 2667–2678 (2005).

23. A. J. Sfeir, W. Chai, J. W. Shay, W. E. Wright, Telomere-end processing: The terminal nucleotides of human chromosomes. *Mol. Cell* **18**, 131–138 (2005).

24. K. H. Choi, A. S. Lakamp-Hawley, C. Kolar, Y. Yan, G. E. O. Borgstahl, M. M. Ouellette, The OB-fold domain 1 of human POT1 recognizes both telomeric and non-telomeric DNA motifs. *Biochimie* **115**, 17–27 (2015).

25. D. M. Baird, J. Rowson, D. Wynford-Thomas, D. Kipling, Extensive allelic variation and ultrashort telomeres in senescent human cells. *Nat. Genet.* **33**, 203–207 (2003).

26. C. J. Lim, A. J. Zaug, H. J. Kim, T. R. Cech, Reconstitution of human shelterin complexes reveals unexpected stoichiometry and dual pathways to enhance telomerase processivity. *Nat. Commun.* **8**, 1075 (2017).

27. T. Paul, W. Liou, X. Cai, P. L. Opresko, S. Myong, TRF2 promotes dynamic and stepwise looping of POT1 bound telomeric overhang. *Nucleic Acids Res.* **49**, 12377–12393 (2021).

28. S. Ray, J. N. Bandaria, M. H. Qureshi, A. Yildiz, H. Balci, G-quadruplex formation in telomeres enhances POT1/TPP1 protection against RPA binding. *Proc. Natl. Acad. Sci. U.S.A.* **111**, 2990–2995 (2014).

29. J. C. Zinder, P. D. B. Olinares, V. Svetlov, M. W. Bush, E. Nudler, B. T. Chait, T. Walz, T. de Lange, Shelterin is a dimeric complex with extensive structural heterogeneity. *Proc. Natl. Acad. Sci. U.S.A.* **119**, e2201662119 (2022).

30. F. Wang, E. R. Podell, A. J. Zaug, Y. Yang, P. Baciu, T. R. Cech, M. Lei, The POT1-TPP1 telomere complex is a telomerase processivity factor. *Nature* **445**, 506–510 (2007).

31. J. Nandakumar, C. F. Bell, I. Weidenfeld, A. J. Zaug, L. A. Leinwand, T. R. Cech, The TEL patch of telomere protein TPP1 mediates telomerase recruitment and processivity. *Nature* **492**, 285–289 (2012).

32. H. He, A. S. Multani, W. Cosme-Blanco, H. Tahara, J. Ma, S. Pathak, Y. Deng, S. Chang, POT1b protects telomeres from end-to-end chromosomal fusions and aberrant homologous recombination. *EMBO J.* **25**, 5180–5190 (2006).

33. H. Takai, A. Smogorzewska, T. de Lange, DNA damage foci at dysfunctional telomeres. *Curr. Biol.* **13**, 1549–1556 (2003).

34. G. Glousker, A. S. Briod, M. Quadroni, J. Lingner, Human shelterin protein POT1 prevents severe telomere instability induced by homology-directed DNA repair. *EMBO J.* **39**, e104500 (2020).

35. J. Jumper, R. Evans, A. Pritzel, T. Green, M. Figurnov, O. Ronneberger, K. Tunyasuvunakool, R. Bates, A. Žídek, A. Potapenko, A. Bridgland, C. Meyer, S. A. A. Kohl, A. J. Ballard, A. Cowie, B. Romera-Paredes, S. Nikolov, R. Jain, J. Adler, T. Back, S. Petersen, D. Reiman, E. Clancy, M. Zielinski, M. Steinegger, M. Pacholska, T. Berghammer, S. Bodenstein, D. Silver, O. Vinyals, A. W. Senior, K. Kavukcuoglu, P. Kohli, D. Hassabis, Highly accurate protein structure prediction with AlphaFold. *Nature* **596**, 583–589 (2021).

36. T. Kibe, M. Zimmermann, T. de Lange, TPP1 Blocks an ATR-Mediated Resection Mechanism at Telomeres. *Mol. Cell* **61**, 236–246 (2016).

37. D. Loayza, T. De Lange, POT1 as a terminal transducer of TRF1 telomere length control. *Nature* **423**, 1013–1018 (2003).

38. C. A. MacDougall, T. S. Byun, C. Van, M. C. Yee, K. A. Cimprich, The structural determinants of checkpoint activation. *Genes Dev.* **21**, 898–903 (2007).

39. M. Day, A. W. Oliver, L. H. Pearl, Structure of the human RAD17-RFC clamp loader and 9-1-1 checkpoint clamp bound to a dsDNA-ssDNA junction. *Nucleic Acids Res.* **50**, 8279–8289 (2022).

40. L. R. Myler, C. G. Kinzig, N. K. Sasi, G. Zakusilo, S. W. Cai, T. de Lange, The evolution of metazoan shelterin. *Genes Dev.* **35**, 1625–1641 (2021).

41. L. A. Klobutcher, M. T. Swanton, P. Donini, D. M. Prescott, All gene-sized DNA molecules in four species of hypotrichs have the same terminal sequence and an unusual 3′ terminus. *Proc. Natl. Acad. Sci. U.S.A.* **78**, 3015–3019 (1981).

42. S. Classen, J. A. Ruggles, S. C. Schultz, Crystal structure of the N-terminal domain of Oxytricha nova telomere end-binding protein alpha subunit both uncomplexed and complexed with telomeric ssDNA. *J. Mol. Biol.* **314**, 1113–1125 (2001).

43. M. Lei, E. R. Podell, P. Baumann, T. R. Cech, DNA self-recognition in the structure of Pot1 bound to telomeric single-stranded DNA. *Nature* **426**, 198–203 (2003).

44. S. Grill, V. M. Tesmer, J. Nandakumar, The N Terminus of the OB Domain of Telomere Protein TPP1 Is Critical for Telomerase Action. *Cell Rep.* **22**, 1132–1140 (2018).

45. E. Mossessova, C. D. Lima, Ulp1-SUMO crystal structure and genetic analysis reveal conserved interactions and a regulatory element essential for cell growth in yeast. *Mol. Cell* **5**, 865–876 (2000).

46. S. Grill, S. Padmanaban, A. Friedman, E. Perkey, F. Allen, V. M. Tesmer, J. Chase, R. Khoriaty, C. E. Keegan, I. Maillard, J. Nandakumar, TPP1 mutagenesis screens unravel shelterin interfaces and functions in hematopoiesis. *JCI Insight* **6**, e138059 (2021).

47. T. G. Battye, L. Kontogiannis, O. Johnson, H. R. Powell, A. G. Leslie, iMOSFLM: A new graphical interface for diffraction-image processing with MOSFLM. *Acta Crystallogr. D* **67**, 271–281 (2011).

48. M. D. Winn, C. C. Ballard, K. D. Cowtan, E. J. Dodson, P. Emsley, P. R. Evans, R. M. Keegan, E. B. Krissinel, A. G. W. Leslie, A. McCoy, S. J. McNicholas, G. N. Murshudov, N. S. Pannu, E. A. Potterton, H. R. Powell, R. J. Read, A. Vagin, K. S. Wilson, Overview of the CCP4 suite and current developments. *Acta Crystallogr. D* **67**, 235–242 (2011).

49. A. J. McCoy, R. W. Grosse-Kunstleve, P. D. Adams, M. D. Winn, L. C. Storoni, R. J. Read, Phaser crystallographic software. *J. Appl. Crystallogr.* **40**, 658–674 (2007).

50. D. Liebschner, P. V. Afonine, M. L. Baker, G. Bunkóczi, V. B. Chen, T. I. Croll, B. Hintze, L.-W. Hung, S. Jain, A. J. McCoy, N. W. Moriarty, R. D. Oeffner, B. K. Poon, M. G. Prisant, R. J. Read, J. S. Richardson, D. C. Richardson, M. D. Sammito, O. V. Sobolev, D. H. Stockwell, T. C. Terwilliger, A. G. Urzhumtsev, L. L. Videau, C. J. Williams, P. D. Adams, Macromolecular structure determination using X-rays, neutrons and electrons: Recent developments in Phenix. *Acta Crystallogr. D* **75**, 861–877 (2019).

51. P. Emsley, K. Cowtan, Coot: Model-building tools for molecular graphics. *Acta Crystallogr. D* **60**, 2126–2132 (2004).

52. The PyMOL Molecular Graphics System, Version 2.0, https://pymol.org/2/.

53. S. Grill, K. Bisht, V. M. Tesmer, A. N. Shami, S. S. Hammoud, J. Nandakumar, Two Separation-of-Function Isoforms of Human TPP1 Dictate Telomerase Regulation in Somatic and Germ Cells. *Cell Rep.* **27**, 3511–3521.e7 (2019).

54. B. S. Herbert, J. W. Shay, W. E. Wright, Analysis of telomeres and telomerase. *Curr. Protoc. Cell Biol.* **20**, 18.6.1–18.6.20 (2003).

55. J. Nandakumar, E. R. Podell, T. R. Cech, How telomeric protein POT1 avoids RNA to achieve specificity for single-stranded DNA. *Proc. Natl. Acad. Sci. U.S.A.* **107**, 651–656 (2010).